

# A coupled Ericksen/Allen–Cahn model for liquid crystal droplets

Angelique Morvant<sup>a</sup>, Ethan Seal<sup>b</sup>, Shawn W. Walker<sup>c,\*</sup>

<sup>a</sup> Department of Mathematics, Texas A&M University, College Station, TX 77843, United States

<sup>b</sup> Department of Mathematics, The University of North Texas, Denton, TX 76203, United States

<sup>c</sup> Department of Mathematics and Center for Computation and Technology (CCT) Louisiana State University, Baton Rouge, LA 70803, United States



## ARTICLE INFO

### Article history:

Received 12 August 2017

Received in revised form 13 December 2017

Accepted 5 March 2018

Available online 29 March 2018

### Keywords:

Liquid crystals

Finite element method

Ericksen model

Allen–Cahn

Droplets

Defects

## ABSTRACT

We present a model and discretization that couples the Ericksen model of liquid crystals with variable degree of orientation to the Allen–Cahn equations with a mass constraint. The coupled system models liquid crystal droplets with anisotropic surface tension effects due to the liquid crystal molecular alignment. The total energy consists of the Ericksen energy, phase-field (Allen–Cahn) energy, and a weak anchoring energy that couples the liquid crystal to the diffuse interface. We describe our discretization of the total energy along with a method to compute minimizers via a discrete gradient flow algorithm which has a strictly monotone energy decreasing property. Numerical experiments are given in three dimensions that illustrate a wide variety of droplet shapes that result from their interaction with defects.

© 2018 Elsevier Ltd. All rights reserved.

## 1. Introduction

This paper presents a method for solving the Ericksen model coupled to the Allen–Cahn equations [1–3] in order to model the equilibrium shapes of nematic liquid crystal (LC) droplets with anisotropic surface tension [4–6]. LCs have a variety of applications, e.g. electronic displays [7–9], in addition to a host of potential applications in material science [10–25]. To the best of our knowledge, coupling Ericksen to Allen–Cahn has never been done. The main contributions of the paper are the numerical method and the three-dimensional simulations of LC droplets that illustrate the coupled model.

Nematic droplets have been studied at the continuum level, including experiments [26,27], modeling [28–32], and shape minimization of LC droplets [33]. Numerically, molecular dynamics approaches [34,22] and PDE techniques [35–39] have been used to simulate LC droplets at equilibrium as well as dynamics. The above references use either a (regularized) Oseen–Frank type of model or the Landau–deGennes model ( $\mathbf{Q}$ -tensor) [40,6]. Our paper, and [41], is the first to consider the Ericksen model in the context of LC droplets.

Initial studies of dynamics and numerics for the Ericksen model can be found in [42,43]. More recently, a method was developed in [44–46] to solve the Ericksen model without any ad hoc regularization term. The method was justified via  $\Gamma$ -convergence, and simulations were shown in three dimensions illustrating novel defect structures.

In this paper, we present a coupled model that combines the Ericksen model with anisotropic surface tension to model energy minimizing shapes of LC droplets. The rest of the paper is organized as follows. In Section 2, we present the coupled model at the continuous level, and Section 3 describes our discretization of the continuous model using a finite element

\* Corresponding author.

E-mail addresses: [mae4102@tamu.edu](mailto:mae4102@tamu.edu) (A. Morvant), [ethanseal@my.unt.edu](mailto:ethanseal@my.unt.edu) (E. Seal), [walker@math.lsu.edu](mailto:walker@math.lsu.edu) (S.W. Walker).

method. Section 4 presents a gradient flow method for computing minimizers of the discrete energy, and numerical examples in three dimensions are presented in Section 5. We conclude with some discussion in Section 6.

## 2. Coupled model

We couple two energetic models (Ericksen and Allen–Cahn) to obtain an equilibrium model of LC droplets. The Allen–Cahn energy [2,3] models the separation of two immiscible LC phases with anisotropic surface tension between the phases [4,40,47–49,36,35]. The Ericksen energy models the elasticity of the LC medium [5,40,6,42] in each phase.

### 2.1. Phase field representation

Suppose we have a fixed hold-all domain  $\Omega \subset \mathbb{R}^d$  that partitions into two “phases”. For simplicity, we assume both phases contain liquid crystal material, i.e.  $\Omega \equiv \text{int}(\overline{\Omega_{lc}^1} \cup \overline{\Omega_{lc}^2})$ , where  $\Omega_{lc}^i$  is the  $i$ th liquid crystal phase ( $i = 1, 2$ ). In order to avoid dealing with sharp interfaces, we use a phase field function  $\phi : \Omega \rightarrow [-1, +1]$  to represent the coexistence of the two phases, i.e.  $\phi \approx +1$  in  $\Omega_{lc}^1$  and  $\phi \approx -1$  in  $\Omega_{lc}^2$  [50].

### 2.2. Ericksen’s model

The state of the liquid crystal is modeled by a director field  $\mathbf{n} : \Omega \subset \mathbb{R}^d \rightarrow \mathbb{S}^{d-1}$  with unit length, and a scalar field  $s : \Omega \subset \mathbb{R}^d \rightarrow (-\frac{1}{2}, 1)$  called the *degree-of-orientation* [40,46]. Essentially,  $\mathbf{n}$  specifies the averaged *orientation* of LC molecules, and  $s$  represents how well the individual LC molecules are aligned with  $\mathbf{n}$ . The equilibrium state  $(s, \mathbf{n})$  is assumed to minimize a “one-constant” energy.

#### 2.2.1. Ericksen’s one-constant energy

The equilibrium state  $(s, \mathbf{n})$  of the liquid crystal is assumed to minimize the following energy functional:

$$E_{\text{erk}}(s, \mathbf{n}) := \int_{\Omega} (\kappa |\nabla s|^2 + s^2 |\nabla \mathbf{n}|^2) dx, \tag{1}$$

$$E_{\text{bulk}}(s) := \int_{\Omega} \omega(s) dx,$$

where  $\kappa > 0$ . The function  $\omega$  is  $C^2$ , defined on  $-1/2 < s < 1$ , and satisfies [5,51,52]

1.  $\lim_{s \rightarrow 1} \omega(s) = \lim_{s \rightarrow -1/2} \omega(s) = \infty$ ,
2.  $\omega(0) > \omega(s^*) = \min_{s \in [-1/2, 1]} \omega(s) = 0$  for some  $s^* \in (0, 1)$ ,
3.  $\omega'(0) = 0$ .

#### 2.2.2. Theoretical framework

The initial theory for minimizers (and regularity) of (1) was developed in [51,52], where they introduced an auxiliary variable  $\mathbf{u} = s\mathbf{n}$  which allows for rewriting the energy  $E_{\text{erk}}(s, \mathbf{n})$  as

$$E_{\text{erk}}(s, \mathbf{n}) = \tilde{E}_1(s, \mathbf{u}) := \int_{\Omega} ((\kappa - 1)|\nabla s|^2 + |\nabla \mathbf{u}|^2) dx, \tag{2}$$

which derives from the identity  $\mathbf{n}^T \nabla \mathbf{n} = \mathbf{0}^T$  because of the unit length constraint  $|\mathbf{n}| = 1$ . This suggests the following admissible class of solutions (minimizers) to be [51,52]:

$$\mathcal{K} := \{(s, \mathbf{u}) : \Omega \rightarrow (-1/2, 1) \times \mathbb{R}^d : (s, \mathbf{u}) \in [H^1(\Omega)]^{d+1}, \mathbf{u} = s\mathbf{n}, \mathbf{n} \in \mathbb{S}^{d-1}\}. \tag{3}$$

Note: we use an abuse of notation and write  $(s, \mathbf{n})$  in  $\mathcal{K}$  to be equivalent to  $(s, \mathbf{u})$  in  $\mathcal{K}$  with  $\mathbf{u} = s\mathbf{n}$ .

Enforcing boundary conditions on  $(s, \mathbf{u})$  is done in the following way. Let  $(\Gamma_s, \Gamma_{\mathbf{u}})$  be open subsets of  $\partial\Omega$  where we set Dirichlet boundary conditions for  $(s, \mathbf{u})$ . This yields the following restricted admissible class

$$\mathcal{K}(g, \mathbf{r}) := \{(s, \mathbf{u}) \in \mathcal{K} : s|_{\Gamma_s} = g, \mathbf{u}|_{\Gamma_{\mathbf{u}}} = \mathbf{r}\}, \tag{4}$$

for some given functions  $(g, \mathbf{r}) \in [W_{\infty}^1(\mathbb{R}^d)]^{d+1}$  that satisfy the following in a neighborhood of  $\partial\Omega$ :  $-1/2 < g < 1$  and  $\mathbf{r} = g\mathbf{q}$ , for some  $\mathbf{q} \in \mathbb{S}^{d-1}$ . If we further assume

$$g \geq \delta_0 \quad \text{on } \partial\Omega, \quad \text{for some } \delta_0 > 0, \tag{5}$$

then  $\mathbf{n}$  is  $H^1$  in a neighborhood of  $\partial\Omega$  and satisfies  $\mathbf{n} = g^{-1}\mathbf{r} = \mathbf{q} \in \mathbb{S}^{d-1}$  on  $\partial\Omega$ .

If  $s$  is a non-zero constant, the energy  $E_{\text{erk}}(s, \mathbf{n})$  in (1) effectively reduces to the Oseen–Frank energy  $\int_{\Omega} |\nabla \mathbf{n}|^2$ . When  $s$  is variable, it may vanish which relaxes the energy of defects. Indeed, discontinuities in  $\mathbf{n}$  (i.e. defects) may still occur in the singular set

$$S := \{x \in \Omega : s(x) = 0\}, \tag{6}$$

with finite energy:  $E[s, \mathbf{n}] < \infty$ . Existence of minimizers was shown in [51,52]. Some analytical constructions can be found in [40], and several numerical examples are given in [44].

The parameter  $\kappa$  in (1) influences whether defects occur or not. If the boundary condition for  $s$  is positive well away from zero, and if  $\kappa$  is large, then  $\int_{\Omega} \kappa |\nabla s|^2 dx$  dominates the energy and  $s$  stays positive within  $\Omega$ . So, defects are less likely to occur. If  $\kappa$  is small (say  $\kappa < 1$ ), then  $\int_{\Omega} s^2 |\nabla \mathbf{n}|^2 dx$  dominates, so  $s$  may vanish in some regions and induce a defect; see [44,45] for examples of this effect.

### 2.3. Phase field model

#### 2.3.1. Review of Allen–Cahn

LC droplets immersed in an isotropic medium induce an interface  $\partial\Omega_{\text{lc}}$  between the two phases that exhibits surface tension. The energy of the interface  $\Gamma := \partial\Omega_{\text{lc}}$ , assuming a unit surface tension coefficient  $\gamma_0 \equiv 1$ , is given by

$$J(\Gamma) = \int_{\Gamma} \gamma_0 dS = \int_{\Gamma} 1 dS. \tag{7}$$

In the phase field framework [53,50,54], the sharp interface is “smoothed out” and represented by steep transitions of  $\phi$ , i.e. where  $|\nabla \phi|$  is large. Indeed, the surface energy (7) is replaced by a “diffuse” energy

$$E_{\text{gr}}(\phi) = \frac{\epsilon}{2} \int_{\Omega} |\nabla \phi|^2 dx, \tag{8}$$

where  $\epsilon > 0$  is the “layer thickness” of the phase field approximation. The intuition here is that the integrand in (8) approximates a Dirac delta function  $\delta_{\Gamma}$  concentrated on the interface  $\Gamma$ , i.e.

$$\int_{\Gamma} 1 dS = \int_{\Omega} \delta_{\Gamma} dx \approx \int_{\Omega} \frac{\epsilon}{2} |\nabla \phi|^2 dx.$$

Note that the oriented unit normal vector  $\mathbf{v}$  of  $\Gamma$  is approximated by  $\nabla \phi / |\nabla \phi|$ .

In addition to  $E_{\text{gr}}$ , a mixing energy is added to the total energy to penalize mixing of the two phases:

$$E_{\text{dw}}(\phi) = \frac{1}{\epsilon} \int_{\Omega} f(\phi) dx, \tag{9}$$

where  $f(t) = \frac{1}{4}(1 - t^2)^2$  is a double-well potential. Combining (8) and (9) yields the standard Allen–Cahn energy:

$$E_{\text{ac}}(\phi) = E_{\text{dw}}(\phi) + E_{\text{gr}}(\phi) = \frac{1}{\epsilon} \int_{\Omega} f(\phi) dx + \frac{\epsilon}{2} \int_{\Omega} |\nabla \phi|^2 dx. \tag{10}$$

The admissible class for  $\phi$  is simply  $H^1(\Omega)$  without any boundary conditions imposed.

#### 2.3.2. Anisotropic surface tension

For LC droplets, the orientation of the LC molecules are influenced by the two-phase interface. This is usually modeled by adding a weak anchoring energy to the total energy of the system [40]. In the sharp interface setting, one adds an energy of the form

$$E = \int_{\Gamma} \gamma(\mathbf{v}) dS,$$

where  $\mathbf{v}$  is the oriented unit normal vector of  $\Gamma$ . One possible choice for  $\gamma$  is given by [40]:

$$\gamma(\mathbf{v}, \mathbf{n}) = \alpha_{\perp} (\mathbf{v} \cdot \mathbf{n})^2 + \alpha_{\parallel} [1 - (\mathbf{v} \cdot \mathbf{n})^2], \quad \alpha_{\perp}, \alpha_{\parallel} \geq 0, \tag{11}$$

where the first (second) term tends to make the minimizing director field  $\mathbf{n}$  perpendicular (parallel) to  $\mathbf{v}$ . Therefore, following a similar derivation as for (8), and following [36,35], we arrive at the following weak anchoring energy:

$$E_{\text{anch},\mathbf{n}}(\phi, s, \mathbf{n}) := \frac{\epsilon}{2} \int_{\Omega} s^2 \{ \alpha_{\perp} (\mathbf{n} \cdot \nabla \phi)^2 + \alpha_{\parallel} [|\mathbf{n}|^2 |\nabla \phi|^2 - (\mathbf{n} \cdot \nabla \phi)^2] \} dx, \tag{12}$$

where we included the degree-of-orientation  $s$  to model a loss of anisotropy when orientational order vanishes. Note that the integral is weighted by  $\epsilon$  so that it scales similarly to (8).

Lastly, we also add an energetic term penalizing  $s$  to agree with  $s^*$  on the diffuse interface:

$$E_{\text{anch},s}(\phi, s) := \frac{\epsilon}{2} \int_{\Omega} (s - s^*)^2 |\nabla \phi|^2 dx, \tag{13}$$

which is needed to ensure that  $s$  does not trivially vanish on the interface, and so cause (12) to vanish as well.

### 2.3.3. Incompressible droplets

We assume the LC droplets, as well as the surrounding isotropic medium are incompressible, i.e. their total volume is conserved. It is well known [53,50] that the  $H^{-1}$  gradient flow of the energy (10) preserves the total volume in the sense that  $\int_{\Omega} \phi(t, x) dx = \int_{\Omega} \phi(0, x) dx$ , for all  $t \geq 0$ , where  $t$  is the gradient flow “time” variable.

In this paper, we are only concerned with the final energy minimizing shapes of LC droplets (not the gradient flow history). Thus, we use a simpler  $L^2$  gradient flow to evolve the phase variable  $\phi$ , simultaneously with the LC variables (see Section 4). However, the  $L^2$  gradient flow does not preserve the volume, so we add the following constraint to enforce volume conservation:

$$\int_{\Omega} \phi dx = \int_{\Omega} \phi_0 dx, \tag{14}$$

where  $\phi_0$  represents the initial distribution of the two phases. This gives the following admissible set for the Allen–Cahn variable  $\phi$ :

$$\mathcal{U}(\phi_0) = \left\{ \phi \in H^1(\Omega) : \int_{\Omega} (\phi - \phi_0) dx = 0 \right\}. \tag{15}$$

### 2.4. Total energy

We seek to minimize the total energy:

$$\begin{aligned} \mathcal{E}(\phi, s, \mathbf{n}) = & W_{\text{erk}} E_{\text{erk}}(s, \mathbf{n}) + W_{\text{bulk}} E_{\text{bulk}}(s) + (W_{\text{ac}} + 2W_{\text{anch}}) E_{\text{dw}}(\phi) + W_{\text{ac}} E_{\text{gr}}(\phi) \\ & + W_{\text{anch}} [E_{\text{anch}, \mathbf{n}}(\phi, s, \mathbf{n}) + E_{\text{anch}, s}(\phi, s)], \end{aligned} \tag{16}$$

over all  $(\phi, s, \mathbf{n})$  in the admissible set  $\mathcal{A} := \mathcal{U}(\phi_0) \times \mathcal{K}(g, \mathbf{r})$ . The weighting parameters  $W_{\text{erk}}$ ,  $W_{\text{bulk}}$ ,  $W_{\text{ac}}$ ,  $W_{\text{anch}}$  are all positive constants. Note that since  $E_{\text{gr}}$ ,  $E_{\text{anch}, \mathbf{n}}$ , and  $E_{\text{anch}, s}$  all scale with  $\epsilon |\nabla \phi|^2$ , we choose the weight for  $E_{\text{dw}}$  to be  $W_{\text{ac}} + 2W_{\text{anch}}$ . This is done to ensure that mixing and diffusion are of comparable magnitude; otherwise, if  $E_{\text{dw}}$  is not sufficiently penalized then the droplets will “diffuse away”.

## 3. Discretization

We state how the continuous energies in (16) are approximated and give the variational derivatives of the discrete energies, which are needed in the gradient flow scheme.

In order to streamline the development of the method, we adopt some notational conveniences. Let  $(\cdot, \cdot) : L^2(\Omega) \times L^2(\Omega) \rightarrow \mathbb{R}$  be the  $L^2(\Omega)$  inner product, and  $a(\cdot, \cdot) : H^1(\Omega) \times H^1(\Omega) \rightarrow \mathbb{R}$  be the  $H^1(\Omega)$  inner product, i.e.

$$(u, v) = \int_{\Omega} uv, \quad (\mathbf{v}, \mathbf{w}) = \int_{\Omega} \mathbf{v} \cdot \mathbf{w}, \quad a(u, v) = \int_{\Omega} \nabla u \cdot \nabla v, \quad a(\mathbf{v}, \mathbf{w}) = \int_{\Omega} \nabla \mathbf{v} \cdot \nabla \mathbf{w}.$$

### 3.1. Domain mesh

We discretize the domain  $\Omega$  with a conforming simplicial triangulation  $\mathcal{T}_h = \{T\}$ . The set of nodes (vertices) of  $\mathcal{T}_h$  is denoted  $\mathcal{N}_h$ ; the number of nodes is  $n$ . We require  $\mathcal{T}_h$  to be *weakly acute*, namely

$$k_{ij} := - \int_{\Omega} \nabla \eta_i \cdot \nabla \eta_j dx \equiv -a(\eta_i, \eta_j) \geq 0 \quad \text{for all } i \neq j, \tag{17}$$

where  $\{\eta_i\}$  are standard “hat” basis functions, with  $\eta_i$  associated with node  $x_i \in \mathcal{N}_h$ . This condition is necessary in order to guarantee that the discrete Ericksen energy (21) is positive semi-definite and has a monotonicity property with respect to normalizing the director field (see Lemma 2).

The condition (17) imposes a restriction on the mesh  $\mathcal{T}_h$  [55,56] (which is severe in three dimensions). For  $d = 2$ , one can characterize (17) as follows.

**Lemma 1 (Weak Acuteness in Two Dimensions).** *For any pair of triangles  $T_1, T_2$  in  $\mathcal{T}_h$  in two space dimensions that share a common edge  $e$ , let  $\alpha_i$  be the angle in  $T_i$  opposite to  $e$  (for  $i = 1, 2$ ). Then (17) holds if and only if  $\alpha_1 + \alpha_2 \leq 180^\circ$  for every edge  $e$ .*

Generalizations of Lemma 1 to three dimensions, involving interior dihedral angles of tetrahedra, can be found in [57,58]. We point out that a *non-obtuse* mesh, which is automatically weakly-acute, of a simple rectangular region is simple to generate.

### 3.2. Ericksen

#### 3.2.1. Finite element spaces

We define the following finite element spaces on the mesh  $\mathcal{T}_h$ :

$$\begin{aligned} \mathbb{S}_h &:= \{s_h \in H^1(\Omega) : s_h|_T \text{ is affine for all } T \in \mathcal{T}_h\}, \\ \mathbb{U}_h &:= \{\mathbf{u}_h \in [H^1(\Omega)]^d : \mathbf{u}_h|_T \text{ is affine in each component for all } T \in \mathcal{T}_h\}, \\ \mathbb{N}_h &:= \{\mathbf{n}_h \in \mathbb{U}_h : |\mathbf{n}_h(x_i)| = 1 \text{ for all nodes } x_i \in \mathcal{N}_h\}, \end{aligned} \tag{18}$$

where  $\mathbb{N}_h$  imposes the unit length constraint *at the nodes* of the mesh.

Let  $I_h$  be the Lagrange interpolation operator for either  $\mathbb{S}_h$  or  $\mathbb{U}_h$ . With this, we define the following *discrete* version of the admissible class:

$$\mathcal{K}_h := \{(s_h, \mathbf{u}_h) \in \mathbb{S}_h \times \mathbb{U}_h : -1/2 < s_h < 1 \text{ in } \Omega, \mathbf{u}_h = I_h(s_h \mathbf{n}_h) \text{ where } \mathbf{n}_h \in \mathbb{N}_h\}. \tag{19}$$

Next, take  $g_h := I_h g$  and  $\mathbf{r}_h := I_h \mathbf{r}$  to be the discrete Dirichlet data, and define the discrete spaces that include (Dirichlet) boundary conditions

$$\mathbb{S}_h(\Gamma_s, g_h) := \{s_h \in \mathbb{S}_h : s_h|_{\Gamma_s} = g_h\}, \quad \mathbb{U}_h(\Gamma_u, \mathbf{r}_h) := \{\mathbf{u}_h \in \mathbb{U}_h : \mathbf{u}_h|_{\Gamma_u} = \mathbf{r}_h\},$$

as well as the discrete admissible class with boundary conditions:

$$\mathcal{K}_h(g_h, \mathbf{r}_h) := \{(s_h, \mathbf{u}_h) \in \mathcal{K}_h : s_h \in \mathbb{S}_h(\Gamma_s, g_h), \mathbf{u}_h \in \mathbb{U}_h(\Gamma_u, \mathbf{r}_h)\}. \tag{20}$$

Again, we use the abuse of notation where  $(s_h, \mathbf{n}_h)$  in  $\mathcal{K}_h(g_h, \mathbf{r}_h)$  is equivalent to  $(s_h, \mathbf{u}_h)$  in  $\mathcal{K}_h(g_h, \mathbf{r}_h)$  with  $\mathbf{u}_h = I_h(s_h \mathbf{n}_h)$ . Note that, because of (5), we can impose the Dirichlet condition  $\mathbf{n}_h = I_h[g_h^{-1} \mathbf{r}_h]$  on  $\partial\Omega$ .

#### 3.2.2. Energy

The discrete form of the Ericksen energy  $E_{\text{erk}}$  is given by

$$E_{\text{erk}}^h(s_h, \mathbf{n}_h) := \kappa \int_{\Omega} |\nabla s_h|^2 dx + \frac{1}{2} \sum_{i,j=1}^n k_{ij} \left( \frac{s_h(x_i)^2 + s_h(x_j)^2}{2} \right) |\mathbf{n}_h(x_i) - \mathbf{n}_h(x_j)|^2, \tag{21}$$

which was derived and analyzed in [44]; note that the second term is a  $O(h)$  approximation of  $\int_{\Omega} s^2 |\nabla \mathbf{n}|^2$ . The advantage of the discrete form is that it can handle the (nodal) unit length constraint as well as the degeneracy of the model without regularization; see [44] for more information.

It is convenient to rewrite  $E_{\text{erk}}^h$  with a multi-linear form. Define  $e(\cdot, \cdot; \cdot, \cdot) : \mathbb{S}_h \times \mathbb{S}_h \times \mathbb{U}_h \times \mathbb{U}_h \rightarrow \mathbb{R}$  by

$$\begin{aligned} e(s_h, z_h; \mathbf{v}_h, \mathbf{w}_h) &:= \sum_{i,j=1}^N k_{ij} \left( \frac{s_h(x_i)z_h(x_i) + s_h(x_j)z_h(x_j)}{2} \right) \\ &\quad \cdot (\mathbf{v}_h(x_i) - \mathbf{v}_h(x_j)) \cdot (\mathbf{w}_h(x_i) - \mathbf{w}_h(x_j)), \end{aligned} \tag{22}$$

which is linear in each argument. Thus,

$$E_{\text{erk}}^h(s_h, \mathbf{n}_h) = \kappa a(s_h, s_h) + \frac{1}{2} e(s_h, s_h; \mathbf{n}_h, \mathbf{n}_h), \tag{23}$$

and the first variational derivatives are given by

$$\delta_{\mathbf{n}_h} E_{\text{erk}}^h(s_h, \mathbf{n}_h; \mathbf{w}_h) = e(s_h, s_h; \mathbf{n}_h, \mathbf{w}_h), \tag{24}$$

$$\delta_{s_h} E_{\text{erk}}^h(s_h, \mathbf{n}_h; z_h) = 2\kappa a(s_h, z_h) + e(s_h, z_h; \mathbf{n}_h, \mathbf{n}_h). \tag{25}$$

As was shown in [44],  $E_{\text{erk}}^h$  satisfies the following monotonicity property with respect to the unit length constraint.

**Lemma 2.** Let  $E_{\text{erk}}^h(s_h, \mathbf{n}_h)$  be defined by (23) and assume the mesh  $\mathcal{T}_h$  satisfies (17). If  $|\mathbf{n}_h(x_i)| \geq 1$  at all nodes  $x_i$  in  $\mathcal{N}_h$ , then

$$E_{\text{erk}}^h(s_h, \mathbf{n}_h) \geq E_{\text{erk}}^h\left(s_h, \frac{\mathbf{n}_h}{|\mathbf{n}_h|}\right).$$

The double well energy is discretized in a standard way:

$$E_{\text{bulk}}^h(s_h) := \int_{\Omega} \omega(s_h) dx, \tag{26}$$

where  $\phi_h \in \mathcal{U}_h(\phi_0)$  is discussed in Section 3.3. The variational derivative of  $E_{\text{bulk}}^h$  is approximated by a convex splitting technique [59,54,60] for time-stepping purposes. First, we split  $\omega$  into a convex and a concave part, i.e. let  $\omega_c, \omega_e$  be convex functions for all  $s \in (-1/2, 1)$  so that  $\omega(s) = \omega_c(s) - \omega_e(s)$ . Then set

$$\delta_{s_h} E_{\text{bulk}}^h(s_h^{k+1}; z_h) := ([\omega'_c(s_h^{k+1}) - \omega'_e(s_h^k)], z_h), \tag{27}$$

which yields the inequality

$$E_{\text{bulk}}^h(s_h^{k+1}) - E_{\text{bulk}}^h(s_h^k) \leq \delta_{s_h} E_{\text{bulk}}^h(s_h^{k+1}; s_h^{k+1} - s_h^k), \tag{28}$$

for any  $s_h^k$  and  $s_h^{k+1}$  in  $\mathbb{S}_h$  [44].

### 3.3. Allen–Cahn

We introduce the discrete version of (15):

$$\mathcal{U}_h(\phi_{h,0}) = \left\{ \phi_h \in \mathbb{S}_h : \int_{\Omega} (\phi_h - \phi_{h,0}) dx = \mathbf{0} \right\}, \tag{29}$$

where  $\phi_{h,0}$  represents the (discrete) initial distribution of the two phases (e.g.  $\phi_{h,0} = I_h \phi_0$ ); thus, we replace  $\phi$  by  $\phi_h$  in  $\mathcal{U}_h(\phi_{h,0})$ . The standard Allen–Cahn energy terms, as well as  $E_{\text{anch},s}$ , are discretized in the usual way:

$$E_{\text{dw}}^h(\phi_h) := E_{\text{dw}}(\phi_h), \quad E_{\text{gr}}^h(\phi_h) := E_{\text{gr}}(\phi_h), \quad E_{\text{anch},s}^h(\phi_h, s_h) := E_{\text{anch},s}(\phi_h, s_h), \tag{30}$$

with variational derivatives given by

$$\begin{aligned} \delta_{\phi_h} E_{\text{gr}}^h(\phi_h; \psi_h) &:= \epsilon a(\phi_h, \psi_h), \\ \delta_{\phi_h} E_{\text{anch},s}^h(\phi_h, s_h; \psi_h) &:= \epsilon ((s_h - s^*)^2 \nabla \phi_h, \nabla \psi_h), \\ \delta_{s_h} E_{\text{anch},s}^h(\phi_h, s_h; z_h) &:= \epsilon (|\nabla \phi_h|^2 (s_h - s^*), z_h). \end{aligned} \tag{31}$$

We discretize the double well  $f$  for the phase variable similar to  $\omega$ , i.e. we write

$$f(t) = \frac{1}{4}(1 - 2t^2 + t^4) = \frac{1}{4}(1 + \xi_0 t^2) - \frac{1}{4}[(2 + \xi_0)t^2 - t^4] =: f_c(t) - f_e(t), \tag{32}$$

where  $\xi_0 > 0$  is sufficiently large. Then define

$$\delta_{\phi_h} E_{\text{dw}}^h(\phi_h^{k+1}; \psi_h) := \frac{1}{\epsilon} \int_{\Omega} [f'_c(\phi_h^{k+1}) - f'_e(\phi_h^k)] \psi_h \, dx, \tag{33}$$

which yields the inequality

$$E_{\text{dw}}^h(\phi_h^{k+1}) - E_{\text{dw}}^h(\phi_h^k) \leq \delta_{\phi_h} E_{\text{dw}}^h(\phi_h^{k+1}; \phi_h^{k+1} - \phi_h^k), \tag{34}$$

for all  $\phi_h^k$  and  $\phi_h^{k+1}$  in  $\mathbb{S}_h$  [59,54,60].

The anisotropic anchoring energy  $E_{\text{anch},\mathbf{n}}$  is handled using a “lumped” approach. Define the multi-linear form  $c : \mathbb{U}_h \times \mathcal{P}_0 \times \mathbb{U}_h \times \mathcal{P}_0 \times \mathbb{S}_h \times \mathbb{S}_h \rightarrow \mathbb{R}$ , where  $\mathcal{P}_0$  is the space of piecewise constant, vector-valued functions such that

$$\begin{aligned} c_{\perp}(\mathbf{v}_h, \nabla \phi_h, \mathbf{w}_h, \nabla \psi_h; s_h, z_h) &:= \sum_{T_j \subset \mathcal{T}_h} \int_{T_j} I_h \{ (s_h z_h) (\mathbf{v}_h \cdot \nabla \phi_h) (\mathbf{w}_h \cdot \nabla \psi_h) \}, \\ c_{\parallel}(\mathbf{v}_h, \nabla \phi_h, \mathbf{w}_h, \nabla \psi_h; s_h, z_h) &:= \sum_{T_j \subset \mathcal{T}_h} \int_{T_j} I_h \{ (s_h z_h) [(\mathbf{v}_h \cdot \mathbf{w}_h) (\nabla \phi_h \cdot \nabla \psi_h) - (\mathbf{v}_h \cdot \nabla \phi_h) (\mathbf{w}_h \cdot \nabla \psi_h)] \}, \end{aligned} \tag{35}$$

where  $I_h$  is the Lagrange interpolant. The finite element realization of (35) depends on which variables are held fixed; in any case, the result is a block matrix, where each block is an  $N \times N$  diagonal matrix.

With this, we define the discrete anchoring condition as

$$E_{\text{anch},\mathbf{n}}^h(\phi_h, s_h, \mathbf{n}_h) = \frac{\epsilon}{2} [\alpha_{\perp} c_{\perp}(\mathbf{n}_h, \nabla \phi_h, \mathbf{n}_h, \nabla \phi_h; s_h, s_h) + \alpha_{\parallel} c_{\parallel}(\mathbf{n}_h, \nabla \phi_h, \mathbf{n}_h, \nabla \phi_h; s_h, s_h)]. \tag{36}$$

Using [46, Lemma 6],  $E_{\text{anch},\mathbf{n}}^h$  satisfies the following monotonicity property with respect to the unit length constraint.

**Lemma 3.** Let  $E_{\text{anch},\mathbf{n}}^h(\phi_h, s_h, \mathbf{n}_h)$  be defined by (36). If  $|\mathbf{n}_h(x_i)| \geq 1$  at all nodes  $x_i$  in  $\mathcal{N}_h$ , then

$$E_{\text{anch},\mathbf{n}}^h(\phi_h, s_h, \mathbf{n}_h) \geq E_{\text{anch},\mathbf{n}}^h\left(\phi_h, s_h, \frac{\mathbf{n}_h}{|\mathbf{n}_h|}\right).$$

The variational derivatives are as follows:

$$\begin{aligned} \delta_{\phi_h} E_{\text{anch},\mathbf{n}}^h(\phi_h, s_h, \mathbf{n}_h; \psi_h) &= \epsilon \left[ \alpha_{\perp} c_{\perp}(\mathbf{n}_h, \nabla \phi_h, \mathbf{n}_h, \nabla \psi_h; s_h, s_h) + \alpha_{\parallel} c_{\parallel}(\mathbf{n}_h, \nabla \phi_h, \mathbf{n}_h, \nabla \psi_h; s_h, s_h) \right], \\ \delta_{s_h} E_{\text{anch},\mathbf{n}}^h(\phi_h, s_h, \mathbf{n}_h; z_h) &= \epsilon \left[ \alpha_{\perp} c_{\perp}(\mathbf{n}_h, \nabla \phi_h, \mathbf{n}_h, \nabla \phi_h; s_h, z_h) + \alpha_{\parallel} c_{\parallel}(\mathbf{n}_h, \nabla \phi_h, \mathbf{n}_h, \nabla \phi_h; s_h, z_h) \right], \\ \delta_{\mathbf{n}_h} E_{\text{anch},\mathbf{n}}^h(\phi_h, s_h, \mathbf{n}_h; \mathbf{v}_h) &= \epsilon \left[ \alpha_{\perp} c_{\perp}(\mathbf{n}_h, \nabla \phi_h, \mathbf{v}_h, \nabla \phi_h; s_h, s_h) + \alpha_{\parallel} c_{\parallel}(\mathbf{n}_h, \nabla \phi_h, \mathbf{v}_h, \nabla \phi_h; s_h, s_h) \right], \end{aligned} \tag{37}$$

which follow from the (multi-)linearity and symmetry of  $c_{\perp}, c_{\parallel}$ .

### 3.4. Total discrete energy

The discrete formulation is as follows. Define the admissible set  $\mathcal{A}_h := \mathcal{U}_h(\phi_{h,0}) \times \mathcal{K}_h(g_h, \mathbf{r}_h)$  and find  $(\phi_h, s_h, \mathbf{n}_h) \in \mathcal{A}_h$  such that the following energy is minimized:

$$\begin{aligned} \mathcal{E}^h(\phi_h, s_h, \mathbf{n}_h) &= W_{\text{erk}} E_{\text{erk}}^h(s_h, \mathbf{n}_h) + W_{\text{bulk}} E_{\text{bulk}}^h(s_h) + (W_{\text{ac}} + 2W_{\text{anch}}) E_{\text{dw}}^h(\phi_h) + W_{\text{ac}} E_{\text{gr}}^h(\phi_h) \\ &\quad + W_{\text{anch}} \left[ E_{\text{anch},\mathbf{n}}^h(\phi_h, s_h, \mathbf{n}_h) + E_{\text{anch},s}^h(\phi_h, s_h) \right]. \end{aligned} \tag{38}$$

## 4. Energy minimization scheme

We minimize the discrete energy  $\mathcal{E}^h(\phi_h, s_h, \mathbf{n}_h)$  by an alternating direction method, i.e. we take gradient descent steps with respect to  $\mathbf{n}_h$ , then with respect to  $s_h$ , and then finally with respect to  $\phi_h$ . This procedure is iterated until numerical convergence is reached. To this end, we introduce a “step-size”  $\delta t > 0$  that is used when decreasing the energy in each direction.

**Remark 4.** Gamma-convergence of the discrete Ericksen energy  $E_{\text{erk}}^h(s_h, \mathbf{n}_h) \rightarrow E_{\text{erk}}(s, \mathbf{n})$  has been analyzed in [44,46]. In addition, the Gamma-convergence for a phase-field Cahn–Hilliard/Ericksen model was proved in [41]. The Gamma-convergence of the coupled Allen–Cahn/Ericksen model considered here essentially follows from the same arguments as in [41], and is not repeated here.

We emphasize that  $\Gamma$ -convergence does not provide a rate of convergence. In fact, it only implies convergence of minimizing sequences up to subsequences, unless the limiting problem has a unique minimizer. In general, we do not expect the functional  $\mathcal{E}(\phi, s, \mathbf{n})$  in (16) to have a unique minimizer. In this case, the  $\Gamma$ -convergence result only says that a sequence of *global* discrete minimizers of (38) will converge to a *global* minimizer of (16).

### 4.1. Decrease with respect to director

The director  $\mathbf{n}$  is updated along the tangent space. Thus, we introduce a “tangent space” variation of  $\mathbb{U}_h$  in (18):

$$\mathbb{U}_h^{\perp}(\mathbf{n}_h) = \{\mathbf{v}_h \in \mathbb{U}_h : \mathbf{v}_h(x_i) \cdot \mathbf{n}_h(x_i) = 0, \text{ for all nodes } x_i \in \mathcal{N}_h\}, \tag{39}$$

which preserves the unit length constraint to first order. With this, given  $(s_h^k, \mathbf{n}_h^k)$  in  $\mathcal{K}_h(g_h, \mathbf{r}_h)$ ,  $\phi_h^k$  in  $\mathbb{S}_h$ , we find  $\mathbf{t}_h^k \in \mathbb{U}_h^{\perp}(\mathbf{n}_h^k) \cap H_{\Gamma_n}^1(\Omega)$  such that

$$\rho(\mathbf{t}_h^k, \mathbf{v}_h) = -W_{\text{erk}} \delta_{\mathbf{n}_h} E_{\text{erk}}^h(s_h^k, \mathbf{n}_h^k + \mathbf{t}_h^k; \mathbf{v}_h) - W_{\text{anch}} \delta_{\mathbf{n}_h} E_{\text{anch},\mathbf{n}}^h(\phi_h^k, s_h^k, \mathbf{n}_h^k + \mathbf{t}_h^k; \mathbf{v}_h),$$

or

$$\begin{aligned} \rho(\mathbf{t}_h^k, \mathbf{v}_h) &= -W_{\text{erk}} e(s_h^k, s_h^k; \mathbf{n}_h^k + \mathbf{t}_h^k, \mathbf{v}_h) - W_{\text{anch}} \epsilon \left[ \alpha_{\perp} c_{\perp}(\mathbf{n}_h^k + \mathbf{t}_h^k, \nabla \phi_h^k, \mathbf{v}_h, \nabla \phi_h^k; s_h^k, s_h^k) \right. \\ &\quad \left. + \alpha_{\parallel} c_{\parallel}(\mathbf{n}_h^k + \mathbf{t}_h^k, \nabla \phi_h^k, \mathbf{v}_h, \nabla \phi_h^k; s_h^k, s_h^k) \right], \end{aligned} \tag{40}$$

for all  $\mathbf{v}_h \in \mathbb{U}_h^{\perp}(\mathbf{n}_h^k) \cap H_{\Gamma_n}^1(\Omega)$ , where  $\rho > 0$  is a damping factor. Using standard techniques, [44,46], one can show this decreases the total energy, i.e.  $\mathcal{E}^h(\phi_h^k, s_h^k, \mathbf{n}_h^k + \mathbf{t}_h^k) \leq \mathcal{E}^h(\phi_h^k, s_h^k, \mathbf{n}_h^k)$ .

Next, we apply a simple, node-wise, projection to enforce the unit length constraint, i.e.

$$\mathbf{n}_h^{k+1}(x_i) := \frac{\mathbf{n}_h^k(x_i) + \mathbf{t}_h^k(x_i)}{|\mathbf{n}_h^k(x_i) + \mathbf{t}_h^k(x_i)|} \text{ at all nodes } x_i \in \mathcal{N}_h. \tag{41}$$

This step also decreases the total energy [61,62,44,46], i.e.

$$\mathcal{E}^h(\phi_h^k, s_h^k, \mathbf{n}_h^{k+1}) \leq \mathcal{E}^h(\phi_h^k, s_h^k, \mathbf{n}_h^k + \mathbf{t}_h^k).$$

### 4.2. Decrease with respect to degree-of-orientation

The degree-of-orientation is updated with a standard gradient flow step. Given  $(s_h^k, \mathbf{n}_h^{k+1})$  in  $\mathcal{K}_h(\mathbf{g}_h, \mathbf{r}_h)$ ,  $\phi_h^k$  in  $\mathbb{S}_h$ , we find  $s_h^{k+1}$  in  $\mathbb{S}_h(\Gamma_s, \mathbf{g}_h)$  such that

$$\begin{aligned} \left( \frac{s_h^{k+1} - s_h^k}{\delta t}, z_h \right) &= -W_{\text{erk}} \delta_{s_h} E_{\text{erk}}^h(s_h^{k+1}, \mathbf{n}_h^{k+1}; z_h) - W_{\text{bulk}} \delta_{s_h} E_{\text{bulk}}^h(s_h^{k+1}; z_h) \\ &\quad - W_{\text{anch}} \left[ \delta_{s_h} E_{\text{anch}, \mathbf{n}}^h(\phi_h^k, s_h^{k+1}, \mathbf{n}_h^{k+1}; z_h) + \delta_{s_h} E_{\text{anch}, s}^h(\phi_h^k, s_h^{k+1}; z_h) \right], \end{aligned}$$

or

$$\begin{aligned} \left( \frac{s_h^{k+1} - s_h^k}{\delta t}, z_h \right) &= -W_{\text{erk}} \left[ 2\kappa a(s_h^{k+1}, z_h) + e(s_h^{k+1}, z_h; \mathbf{n}_h^{k+1}, \mathbf{n}_h^{k+1}) \right] \\ &\quad - W_{\text{bulk}} \left( [\omega'_c(s_h^{k+1}) - \omega'_e(s_h^k)], z_h \right) \\ &\quad - W_{\text{anch}} \epsilon \left[ \alpha_{\perp} c_{\perp}(\mathbf{n}_h^{k+1}, \nabla \phi_h^k, \mathbf{n}_h^{k+1}, \nabla \phi_h^k; s_h^{k+1}, z_h) \right. \\ &\quad \quad \left. + \alpha_{\parallel} c_{\parallel}(\mathbf{n}_h^{k+1}, \nabla \phi_h^k, \mathbf{n}_h^{k+1}, \nabla \phi_h^k; s_h^{k+1}, z_h) \right] \\ &\quad - W_{\text{anch}} \epsilon \left( |\nabla \phi_h^k|^2 (s_h^{k+1} - s^*), z_h \right), \end{aligned} \tag{42}$$

for all  $z_h \in \mathbb{S}_h \cap H_{\Gamma_s}^1(\Omega)$ . Again, this step decreases the energy:  $\mathcal{E}^h(\phi_h^k, s_h^{k+1}, \mathbf{n}_h^{k+1}) \leq \mathcal{E}^h(\phi_h^k, s_h^k, \mathbf{n}_h^{k+1})$  [44,46].

### 4.3. Decrease with respect to phase

The phase is updated with a standard gradient flow step, with a constraint imposed by a Lagrange multiplier to enforce volume conservation (recall (29)). Given  $(s_h^{k+1}, \mathbf{n}_h^{k+1})$  in  $\mathcal{K}_h(\mathbf{g}_h, \mathbf{r}_h)$ ,  $\phi_h^k$  in  $\mathcal{U}_h(\phi_{h,0})$ , we find  $\phi_h^{k+1}$  in  $\mathcal{U}_h(\phi_{h,0})$ , and  $\lambda^{k+1}$  in  $\mathbb{R}$ , such that

$$\begin{aligned} \left( \frac{\phi_h^{k+1} - \phi_h^k}{\delta t}, \psi_h \right) &= \frac{\lambda^{k+1}}{\delta t} (1, \psi_h) - W_{\text{ac}} \delta_{\phi_h} E_{\text{gr}}^h(\phi_h^{k+1}; \psi_h) - (W_{\text{ac}} + 2W_{\text{anch}}) \delta_{\phi_h} E_{\text{dw}}^h(\phi_h^{k+1}; \psi_h) \\ &\quad - W_{\text{anch}} \delta_{\phi_h} E_{\text{anch}, \mathbf{n}}^h(\phi_h^{k+1}, s_h^{k+1}, \mathbf{n}_h^{k+1}; \psi_h) - W_{\text{anch}} \delta_{\phi_h} E_{\text{anch}, s}^h(\phi_h^{k+1}, s_h^{k+1}; \psi_h), \end{aligned}$$

$$\frac{1}{\delta t} (\phi_h^{k+1} - \phi_{h,0}, 1) = 0,$$

or

$$\begin{aligned} \left( \frac{\phi_h^{k+1} - \phi_h^k}{\delta t}, \psi_h \right) &= \frac{\lambda^{k+1}}{\delta t} (1, \psi_h) - W_{\text{ac}} \epsilon a(\phi_h^{k+1}, \psi_h) \\ &\quad - \frac{(W_{\text{ac}} + 2W_{\text{anch}})}{\epsilon} \left( [f'_c(\phi_h^{k+1}) - f'_e(\phi_h^k)], \psi_h \right) \\ &\quad - W_{\text{anch}} \epsilon \left[ \alpha_{\perp} c_{\perp}(\mathbf{n}_h^{k+1}, \nabla \phi_h^{k+1}, \mathbf{n}_h^{k+1}, \nabla \psi_h; s_h^{k+1}, s_h^{k+1}) \right. \\ &\quad \quad \left. + \alpha_{\parallel} c_{\parallel}(\mathbf{n}_h^{k+1}, \nabla \phi_h^{k+1}, \mathbf{n}_h^{k+1}, \nabla \psi_h; s_h^{k+1}, s_h^{k+1}) \right] \\ &\quad - W_{\text{anch}} \epsilon \left( (s_h^{k+1} - s^*)^2 \nabla \phi_h^{k+1}, \nabla \psi_h \right), \end{aligned} \tag{43}$$

$$\frac{1}{\delta t} (\phi_h^{k+1} - \phi_{h,0}, 1) = 0,$$

for all  $\psi_h \in \mathbb{S}_h$ .

The saddle-point system (43) can be eliminated by a priori solving for  $\lambda^{k+1}$ . Choosing  $\psi_h = 1$  reduces (43) to

$$\frac{\lambda^{k+1}}{\delta t} = C_{\lambda} f'_c(1)(\phi_h^{k+1}, 1) - C_{\lambda} (f'_e(\phi_h^k), 1), \quad C_{\lambda} := \frac{(W_{\text{ac}} + 2W_{\text{anch}})}{\epsilon |\Omega|}, \tag{44}$$

where we used that  $(\phi_h^{k+1} - \phi_h^k, 1) = 0$ . Plugging (44) into (43) yields the following variational problem: given  $(s_h^{k+1}, \mathbf{n}_h^{k+1})$  in  $\mathcal{K}_h(\mathbf{g}_h, \mathbf{r}_h)$ ,  $\phi_h^k$  in  $\mathcal{U}_h(\phi_{h,0})$ , we find  $\phi_h^{k+1}$  in  $\mathcal{U}_h(\phi_{h,0})$  such that

$$\begin{aligned}
 \left( \frac{\phi_h^{k+1} - \phi_h^k}{\delta t}, \psi_h \right) &= C_\lambda f'_c(1) (1, \psi_h) (\phi_h^{k+1}, 1) - C_\lambda (f'_e(\phi_h^k), 1) (1, \psi_h) \\
 &- W_{ac} \epsilon a (\phi_h^{k+1}, \psi_h) - \frac{(W_{ac} + 2W_{anch})}{\epsilon} ([f'_c(\phi_h^{k+1}) - f'_e(\phi_h^k)], \psi_h) \\
 &- W_{anch} \epsilon \left[ \alpha_\perp c_\perp (\mathbf{n}_h^{k+1}, \nabla \phi_h^{k+1}, \mathbf{n}_h^{k+1}, \nabla \psi_h; s_h^{k+1}, s_h^{k+1}) \right. \\
 &\quad \left. + \alpha_\parallel c_\parallel (\mathbf{n}_h^{k+1}, \nabla \phi_h^{k+1}, \mathbf{n}_h^{k+1}, \nabla \psi_h; s_h^{k+1}, s_h^{k+1}) \right] \\
 &- W_{anch} \epsilon ((s_h^{k+1} - s^*)^2 \nabla \phi_h^{k+1}, \nabla \psi_h),
 \end{aligned} \tag{45}$$

for all  $\psi_h \in \mathbb{S}_h$ . The solution  $\phi_h^{k+1}$  decreases the energy by standard arguments similar to those in [44,46]. In order to handle the “outer-product” term in solving (45), e.g.  $(1, \psi_h) (\phi_h^{k+1}, 1)$ , we used the Sherman–Morrison method.

**Remark 5.** Using a Lagrange multiplier to enforce global mass conservation is convenient because it eliminates the need to solve a modified Cahn–Hilliard system (a fourth order PDE), which gives a conservation law for the change of mass in a given volume. Indeed, with Cahn–Hilliard, mass is not created or destroyed, but simply enters or leaves the (local) volume considered through a boundary flux.

For the purposes of investigating equilibrium phenomena (as done in this paper), a Lagrange multiplier is sufficient. However, in the context of coarsening dynamics [38,39], using Allen–Cahn with a Lagrange multiplier will yield different dynamics than with Cahn–Hilliard.

#### 4.4. Energy decrease

During each iteration of our algorithm, the three steps in Sections 4.1, 4.2, and 4.3 are solved sequentially in a Gauss–Seidel type of approach. Each step is derived from a gradient flow step with respect to one of the variables, followed by applying a semi-implicit “time”-discretization. This has the advantage of removing any time-step restriction while guaranteeing that each step monotonically decreases the energy. Thus, the entire scheme is monotone energy decreasing and so is robust, i.e. the numerical scheme will always produce a (local) minimizer, regardless of the time-step. Of course, in principle, the choice of time-step can affect the minimizer found but we did not experience this.

Other optimization techniques are possible, such as non-linear conjugate gradient or quasi-newton methods [63]. However, one may need to sacrifice robustness when using a faster method.

#### 4.5. Implementation

The resultant algorithm is as follows. Given  $(\phi_h^k, s_h^k, \mathbf{n}_h^k)$ , we solve (in sequence) (40), (41) to obtain  $\mathbf{n}_h^{k+1}$ , followed by (42) to get  $s_h^{k+1}$ , and then (45) to get  $\phi_h^{k+1}$ . We implemented our method using the MATLAB/C++ finite element toolbox FELICITY [64,65]. For all 3-D simulations, we used the algebraic multi-grid solver (AGMG) [66–69] to solve all linear elliptic systems.

### 5. Numerical experiments

We present the results of several simulations that demonstrate the capabilities and limitations of the model. We start with two examples illustrating the effects of homeotropic and planar anchoring, followed by an example of the formation of a lens. Finally, we present the results of two simulations originally intended to produce the Saturn-ring defects. The domain  $\Omega$  in all cases is a unit cube, and all simulations were run on a  $100 \times 100 \times 100$  mesh with  $\epsilon = 0.03$ ,  $W_{erk} = 1$ ,  $W_{bulk} = 100$ ,  $W_{ac} = 1$ ,  $W_{anch} = 20$ , and  $\kappa = 1$ .

#### 5.1. Expelling a defect from a droplet

We simulate a point defect moving to its equilibrium position from inside a droplet with planar anchoring. For this simulation we set  $\alpha_\parallel = 0$ ,  $\alpha_\perp = 1$ , and we start with a point defect at the center of an ellipsoidal droplet in one corner of the domain. The exact initial conditions are

$$\begin{aligned}
 s &= s^* = 0.7, \\
 \mathbf{n}(x, y, z) &= \frac{(x, y, z) - (0.351, 0.32, 0.35)}{|(x, y, z) - (0.351, 0.32, 0.35)|}, \\
 \phi(x, y, z) &= \begin{cases} 1 & \frac{(x - 0.351)^2}{0.22^2} + \frac{(y - 0.32)^2}{0.16^2} + \frac{(z - 0.35)^2}{0.18^2} < 1 \\ -1 & \text{elsewhere on } \Omega. \end{cases}
 \end{aligned}$$

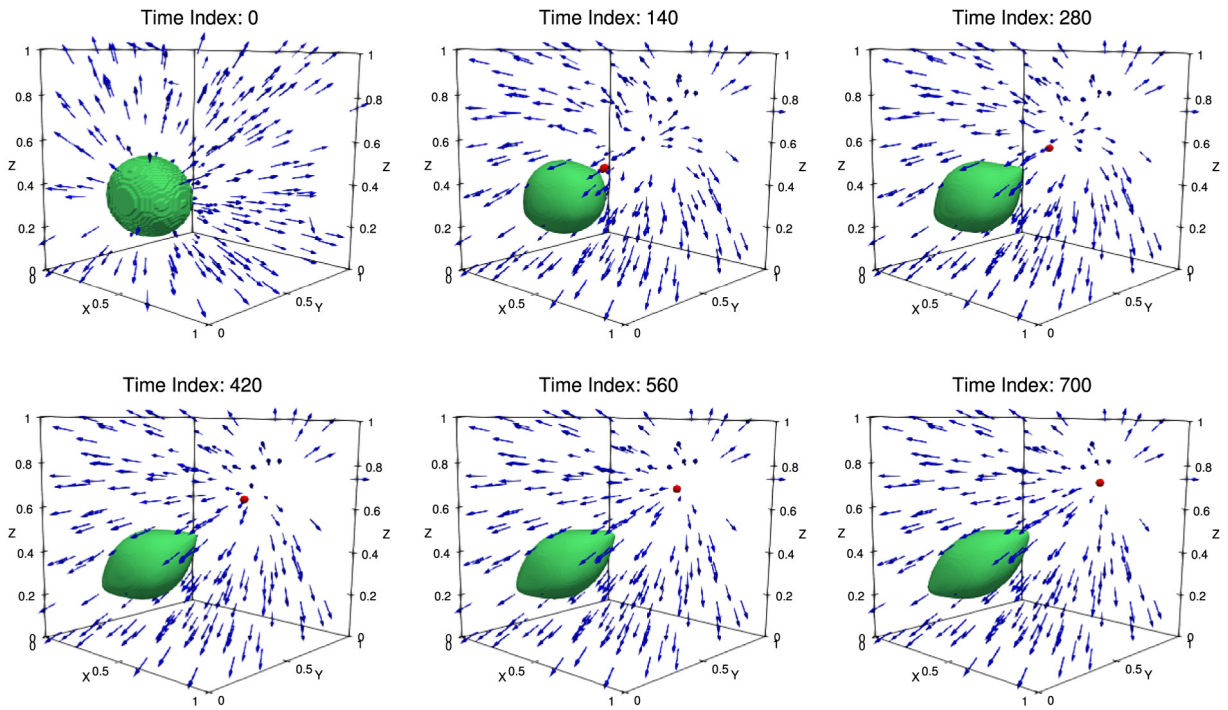


**Fig. 1.** Evolution of the droplet over a period of 700 time steps (Section 5.1). The blue arrows represent the director field, and the green region is the droplet (represented by the  $\phi = 0$  iso-contour). The red “dot” is the  $s = 0.3$  iso-contour, which represents the point defect.

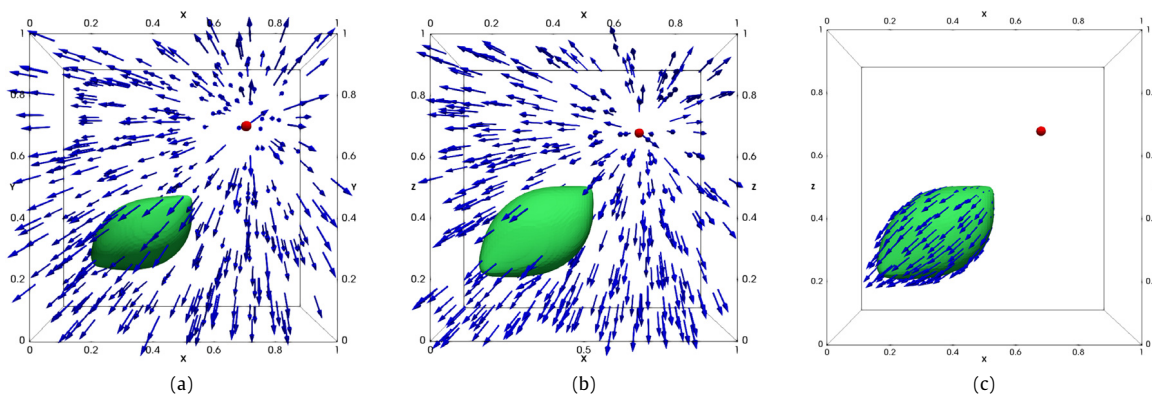


**Fig. 2.** Three views of the final state of the system (Section 5.1). Figs. 2a and 2b show the entire system from the top and side, respectively. Fig. 2c shows the director field (blue arrows) at the surface of the droplet (green). The red “dot” is the  $s = 0.3$  iso-contour, which represents the point defect. The minimum value of  $s$  at the final time step was 0.12.

The boundary conditions for  $s$  are the same as the initial conditions for  $s$ . The boundary conditions for  $\mathbf{n}$  specify a point defect near the upper right-hand corner of the domain:

$$\mathbf{n}(x, y, z) = \frac{(x, y, z) - (0.75, 0.75, 0.75)}{|(x, y, z) - (0.75, 0.75, 0.75)|}$$

The simulation was run with  $\delta t = .05$  for 700 time steps, after which the system essentially attained equilibrium.

The evolution of the droplet is shown in Fig. 1, and several views of the final state of the system are shown in Fig. 2. Since planar anchoring is favored by the droplet, having a point defect inside the droplet is not energetically favorable. Hence, the point defect inside the droplet is expelled and obtains an equilibrium position essentially dictated by the boundary conditions for  $\mathbf{n}$ . The droplet changes shape to best accommodate planar anchoring on the interface. Since the droplet’s boundary is a closed surface, this causes two “corners” to develop. The main “axis” of the droplet is basically aligned with the director field  $\mathbf{n}$ .

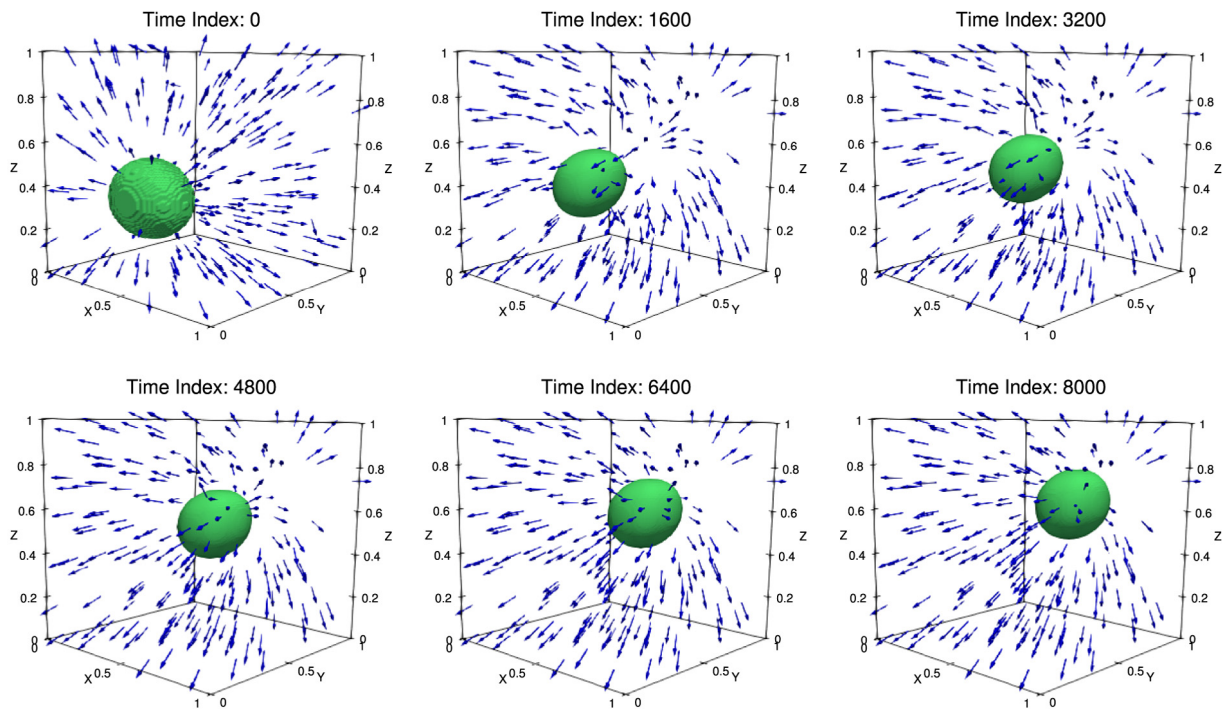


Fig. 3. Evolution of the droplet over 8000 time steps (Section 5.2). Format is the same as Fig. 1.

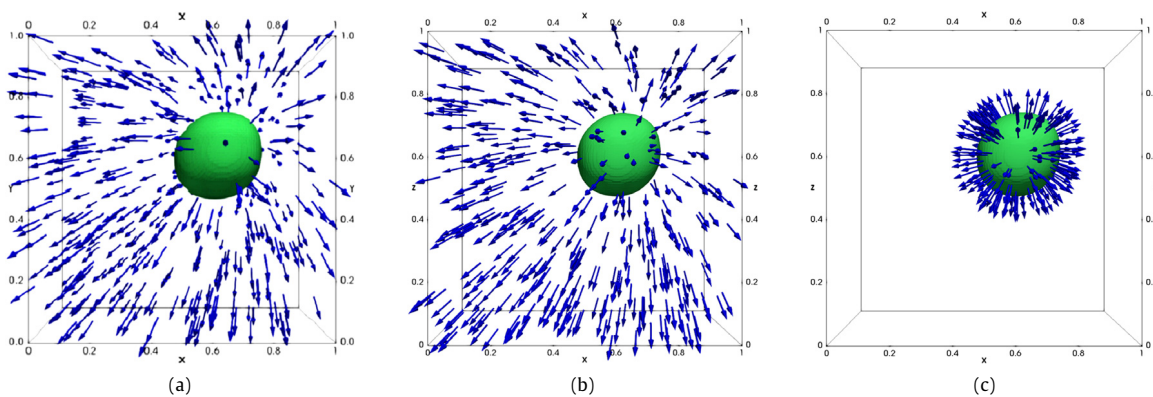


Fig. 4. Three views of the final state of the system (Section 5.2). Figs. 4a and 4b show the entire system from top and side, respectively. Fig. 4c shows the director field at the surface of the droplet. In this case, the director field is perpendicular to the droplet surface in the equilibrium state. The minimum value of  $s$  at the final time step was 0.10.

5.2. Moving a droplet via boundary conditions

We repeat the previous simulation with *homeotropic anchoring*, i.e. we let  $\alpha_{\parallel} = 1$  and  $\alpha_{\perp} = 0$ . The initial and boundary conditions are the same as in the previous section. This simulation was run for 8000 time steps with  $\delta t = 0.05$ .

The evolution of the droplet is shown in Fig. 3, and the final state of the system is shown in Fig. 4. In this case, homeotropic anchoring prevents the defect from escaping the droplet for the following reason. Homeotropic anchoring prefers  $\mathbf{n}$  to be normal to the surface of the droplet. Since the droplet is close to spherical, and a point defect has  $\mathbf{n}$  pointing in a radial fashion, it is energetically favorable for the defect to stay inside the droplet near its center. Note that if  $W_{\text{anch}}$  were much smaller, then this may not necessarily be the case.

Therefore, the droplet (and internal defect) moves toward the upper corner in order to accommodate the (outer) boundary conditions for  $\mathbf{n}$ . Thus, one can position a droplet through appropriate boundary conditions.

### 5.3. Forming a lens

The boundary conditions for  $\mathbf{n}$  can significantly affect the droplet shape, as this example shows. For this simulation, we set  $\alpha_{\parallel} = 1$ ,  $\alpha_{\perp} = 0$ , and we start with a point defect inside a LC droplet of radius 0.2. The exact initial conditions are

$$s = s^* = 0.7,$$

$$\mathbf{n}(x, y, z) = \frac{(x, y, z) - (0.5, 0.5, 0.5)}{|(x, y, z) - (0.5, 0.5, 0.5)|},$$

$$\phi(x, y, z) = \begin{cases} 1 & (x - 0.5)^2 + (y - 0.5)^2 + (z - 0.5)^2 = 0.2^2 \\ -1 & \text{otherwise.} \end{cases}$$

The boundary conditions for  $s$  are the same as the initial conditions for  $s$ . The boundary conditions for the director are simply  $\mathbf{n} = (0, 0, 1)$ . We ran this simulation for 400 time steps with  $\delta t = 0.2$ .

The choice of boundary conditions for  $\mathbf{n}$  and *homeotropic anchoring* on the droplet causes a “frustration” in the director field, which immediately induces a point defect below the droplet (in addition to the point defect inside the droplet). As the gradient flow proceeds, the two point defects move together which acts to further deform the droplet. Eventually, the external point defect enters the droplet and coalesces with the point defect in the center of the droplet (annihilating both defects), and helps to reduce the elastic energy  $E_{\text{erk}}$ . This is shown in Figs. 5 and 6.

### 5.4. Breakup of “Saturn Ring”: homeotropic anchoring

A well-known phenomenon in liquid crystals is the so-called Saturn ring defect [70,71]. The physical setting for its occurrence is to have a rigid inclusion (e.g. a spherical particle in the LC domain) on which strong homeotropic boundary conditions are imposed. The outer boundary conditions are vertical for the director. The result (at equilibrium) is for a line of defect to occur on a circular curve that “orbits” the equator of the particle.

In this example, we investigate how weak anchoring and a deformable droplet affects the LC defect structure. Using the same constants as in Section 5.3, we initialized a point defect at (0.5, 0.5, 0.5) and a LC droplet centered at the same point with a radius of 0.2. The exact initial conditions are

$$s = s^* = 0.7,$$

$$\mathbf{n}(x, y, z) = \frac{(x, y, z) - (0.5, 0.5, 0.5)}{|(x, y, z) - (0.5, 0.5, 0.5)|},$$

$$\phi(x, y, z) = \begin{cases} 1 & (x - 0.5)^2 + (y - 0.5)^2 + (z - 0.5)^2 = 0.2^2 \\ -1 & \text{otherwise.} \end{cases}$$

The boundary conditions for  $s$  are the same as the initial conditions for  $s$ . The boundary conditions for the director are to have  $\mathbf{n}$  pointing inwards along the sides of the domain  $\Omega$ , with a smooth transition to up and down at the top and the bottom of  $\Omega$ ; this is done to avoid having a defect on the outer boundary of the LC domain. We ran this simulation for 900 time steps with  $\delta t = 0.2$ .

However, the Saturn ring does not form (see Figs. 7 and 8). Instead, the ring appears to “breakup” into eight point defects, which slowly coalesce and disappear, with only one point defect remaining. As for the shape of the droplet, the homeotropic anchoring interacts with the single point defect, creating a wedge like shape. The corners (or edges) of the wedge are penalized by the Allen–Cahn energy  $E_{\text{ac}}$ , which results in the slightly rounded wedge (similar to the rounded corners in the previous examples).

In [46], they were able to simulate the Saturn ring when a rigid colloidal particle is included. In their case, weak anchoring (similar to (12), (13)) was also used, but the penalty parameter was more than a factor of 10 higher than our  $W_{\text{anch}}$ . Hence, one can interpret the results in [46] as being for a rigid sphere with (effectively) strong homeotropic anchoring. In order to approximate this setting with our method, we would need to increase  $W_{\text{anch}}$  for “stronger” weak anchoring and increase  $W_{\text{ac}}$  by an even larger amount to force the droplet to stay close to spherical. In addition, we would need to decrease  $\epsilon$  to maintain phase separation in our phase-field model, which would require a much smaller mesh spacing. Unfortunately, this is outside the abilities of our current code implementation.

### 5.5. Breakup of “Saturn ring”: planar anchoring

We ran the same set of conditions as in Section 5.4, except *planar anchoring* is used (i.e.  $\alpha_{\parallel} = 0$ ,  $\alpha_{\perp} = 1$ ). Again, we used 900 time steps with  $\delta t = 0.2$ .

Again, the Saturn ring does not form (see Figs. 9 and 10). The simulation quickly acquires a single point defect. The shape of the droplet is drastically affected. Planar anchoring and the single point defect create a triangular wedge shape (compared to Section 5.4). Moreover, the point defect is along an edge of the droplet, instead of at a corner point. As in Section 5.4, the corners (or edges) of the wedge are penalized by the Allen–Cahn energy  $E_{\text{ac}}$ , which results in a slightly rounded wedge.

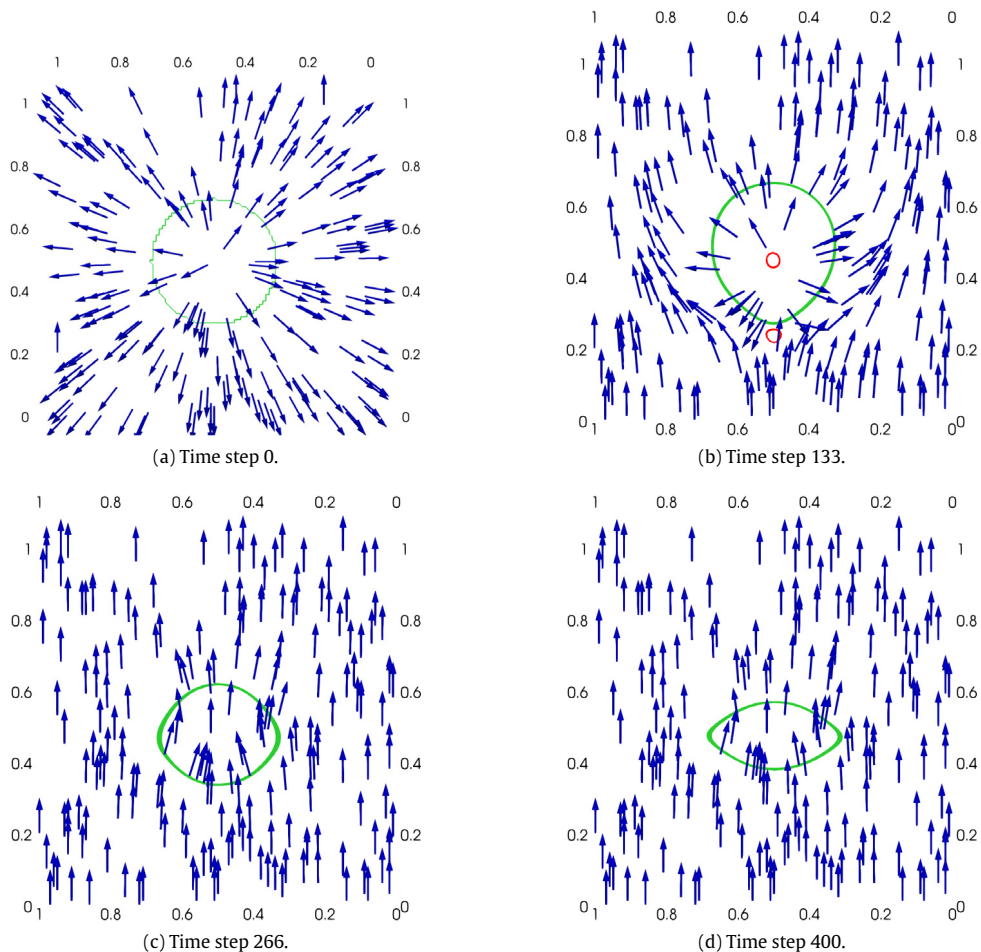


**Fig. 5.** A spherical droplet becoming a lens (Section 5.3). Four two-dimensional slices are shown at various time steps (droplet interface in green). The red circles correspond to the  $s = 0.3$  iso-contour.

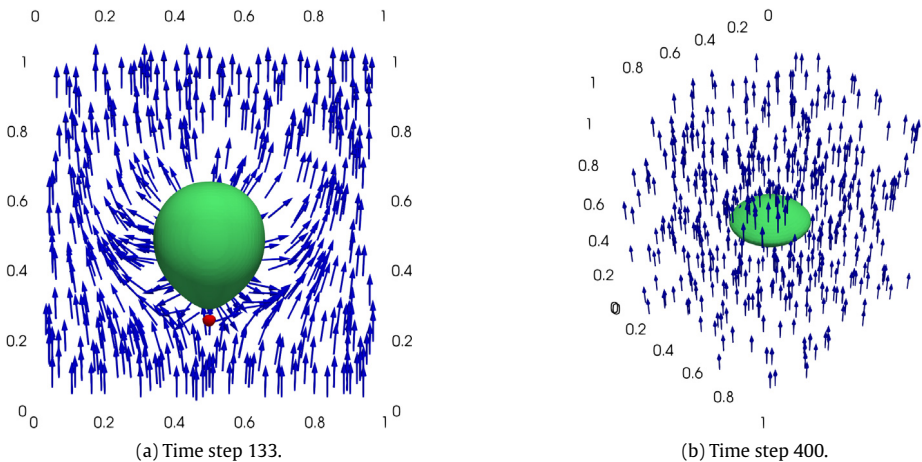


**Fig. 6.** Three dimensional view of lens droplet (Section 5.3). The final droplet shape is an ellipsoidal disk with a “corner” on the lateral side. No defects are present.

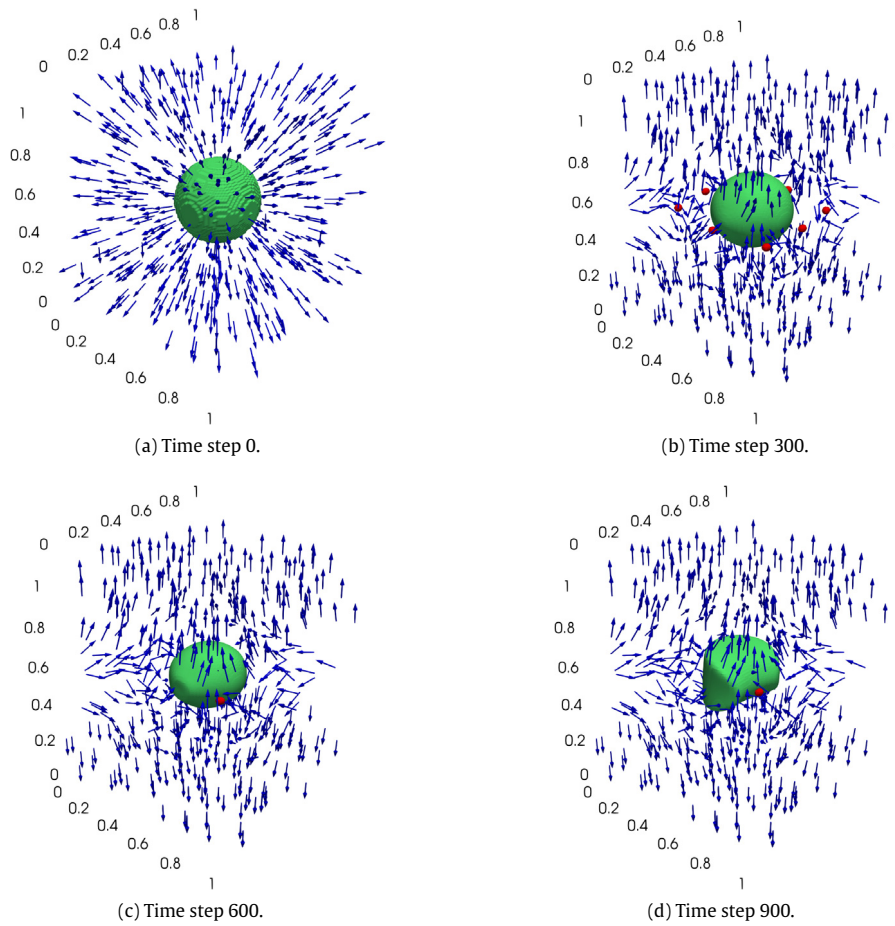


**Fig. 7.** Breakup of Saturn rings: homeotropic anchoring (Section 5.4). Four time steps are shown with arrows representing  $\mathbf{n}$  (droplet is in green). The red “dots” are the  $s = 0.3$  iso-contour, which represents the point defects. The minimum value of  $s$  at the final time step was 0.130037.

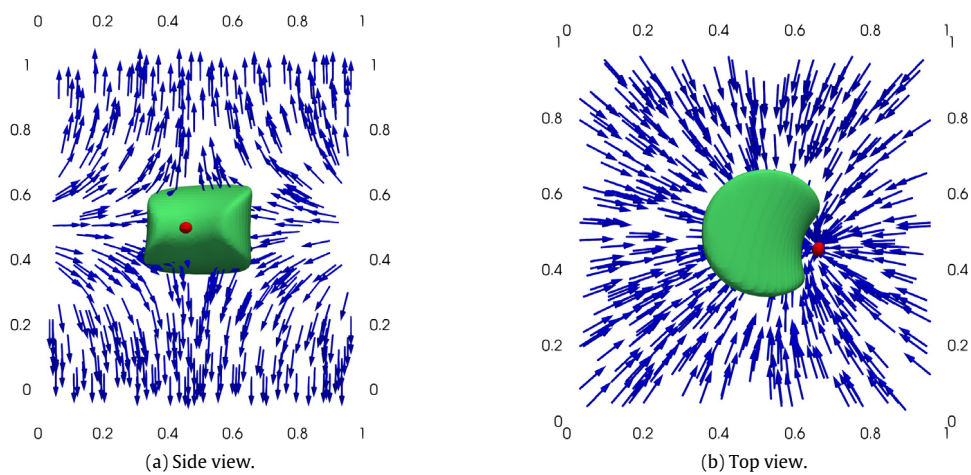


**Fig. 8.** Final views of breakup of Saturn rings: homeotropic anchoring (Section 5.4). Views are from the side and the top at the final time step 900.

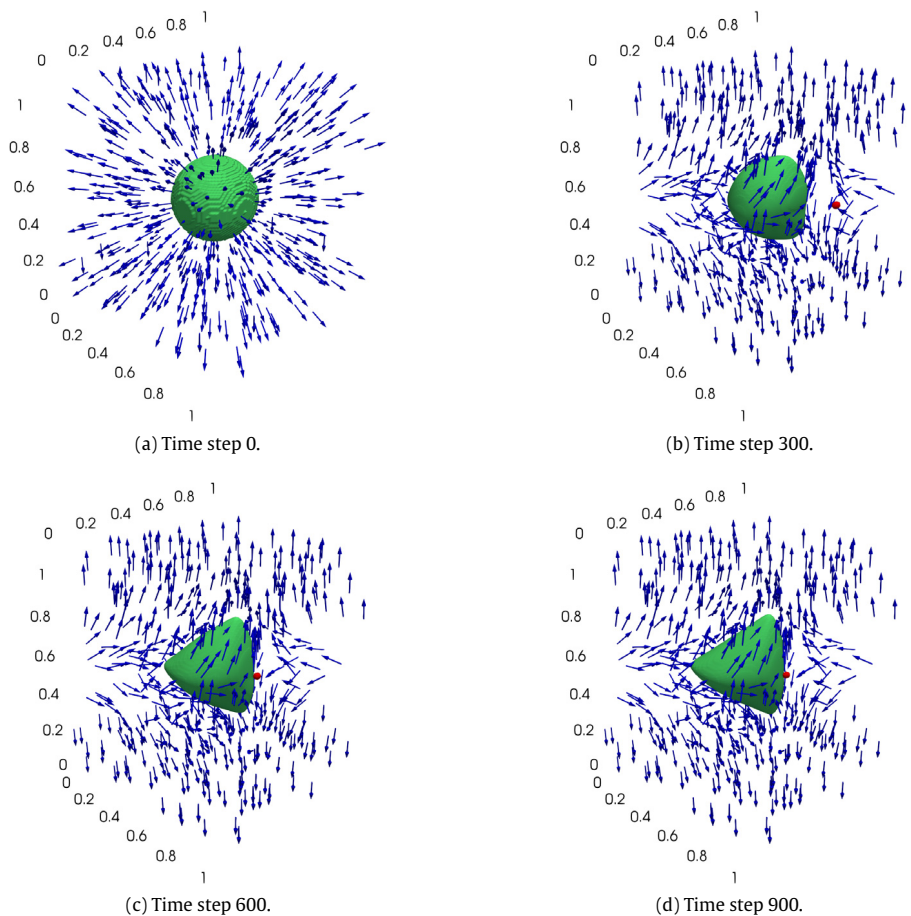


**Fig. 9.** Breakup of Saturn rings: planar anchoring (Section 5.5). Four time steps are shown with arrows representing  $\mathbf{n}$  (droplet is in green). The red “dot” is the  $s = 0.3$  iso-contour, which represents the point defect. The minimum value of  $s$  at the final time step was 0.150222.

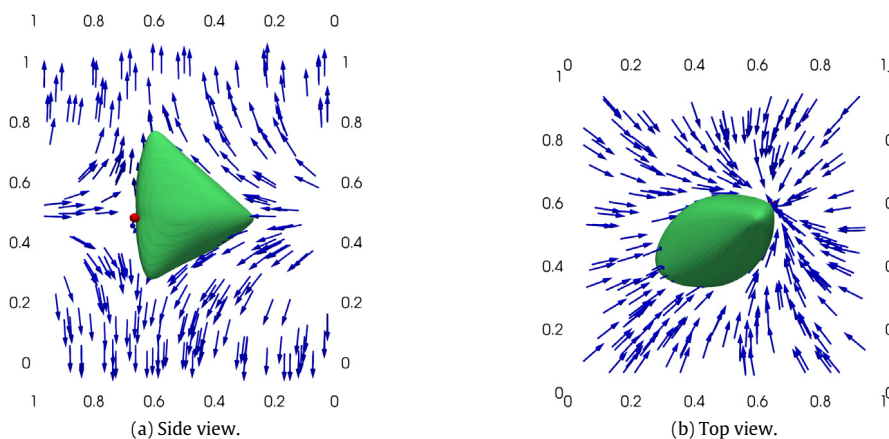


**Fig. 10.** Final views of breakup of Saturn rings: planar anchoring (Section 5.5). Views are from the side and the top at the final time step 900.

## 6. Conclusions

We introduced an Allen–Cahn phase field/Ericksen model and finite element scheme for two-phase nematic LC droplets. We used a gradient flow method to explore gradient flow dynamics for finding energy minimizers. We presented several numerical examples of how LC droplet shapes interact with defects and boundary conditions. Specifically, we showed that droplets can be moved and reshaped by choosing appropriate boundary conditions. Furthermore, droplets can develop faceting and corners or edges. The Saturn ring breakup phenomena suggest some interesting stability questions regarding defects and droplets. For example, how stable is the Saturn ring defect with respect to surface tension forces and anchoring penalty?

This work can be extended to include more general liquid crystal energies, and/or electro-static effects, or even flexoelectric effects. The method could be used to compute optimal shapes of LC droplets, e.g. tactoids [33], nematic droplets on fibers [32], and nematic shells [72]. Another interesting application is to couple Maxwell's equations to the liquid crystal system as a way to model micro lasers based on LC droplets [18].

## Acknowledgments

This material is based upon work supported by the National Science Foundation under award OCI-1560410 (REU) with additional support from the Center for Computation & Technology at Louisiana State University. Computer support is provided by HPC@LSU computing. Walker acknowledges financial support by the NSF via DMS-1418994 and DMS-1555222 (CAREER).

## References

- [1] J.W. Cahn, J.E. Hilliard, Free energy of a nonuniform system. I. Interfacial free energy, *J. Chem. Phys.* 28 (2) (1958) 258–267.
- [2] J.W. Cahn, S.M. Allen, A microscopic theory for domain wall motion and its experimental verification in Fe-Al alloy domain growth kinetics, *J. Phys. Colloq.* 38 (12) (1977). <http://dx.doi.org/10.1051/jphyscol:1977709>. C7-51–C7-54.
- [3] S.M. Allen, J.W. Cahn, A microscopic theory for antiphase boundary motion and its application to antiphase domain coarsening, *Acta Metall.* 27 (6) (1979) 1085–1095. [http://dx.doi.org/10.1016/0001-6160\(79\)90196-2](http://dx.doi.org/10.1016/0001-6160(79)90196-2). URL <http://www.sciencedirect.com/science/article/pii/0001616079901962>.
- [4] B. Jerome, Surface effects and anchoring in liquid crystals, *Rep. Progr. Phys.* 54 (3) (1991) 391. URL <http://stacks.iop.org/0034-4885/54/i=3/a=002>.
- [5] J. Ericksen, Liquid crystals with variable degree of orientation, *Arch. Ration. Mech. Anal.* 113 (2) (1991) 97–120. <http://dx.doi.org/10.1007/BF00380413>.
- [6] P.G. de Gennes, J. Prost, *The Physics of Liquid Crystals*, second ed., in: *International Series of Monographs on Physics*, vol. 83, Oxford Science Publication, Oxford, UK, 1995.
- [7] J.W. Goodby, Chapter introduction to defect textures in liquid crystals, in: Janglin Chen, Wayne Cranton, Mark Fihn (Eds.), *Handbook of Visual Display Technology*, Springer, 2012, pp. 1290–1314.
- [8] R. Perkins, *Liquid Crystal*, Educational Innovations, Inc., 2009. URL [http://www.teachersource.com/downloads/lesson\\_pdf/LC-AST.pdf](http://www.teachersource.com/downloads/lesson_pdf/LC-AST.pdf).
- [9] B. Senyuk, *Liquid crystals: a simple view on a complex matter*, URL <http://www.personal.kent.edu/bisenyuk/liquidcrystals/>, 2010.
- [10] P.J. Ackerman, J. van de Lagemaat, I.I. Smalyukh, Self-assembly and electrostriction of arrays and chains of hopfion particles in chiral liquid crystals, *Nature Commun.* 6 (2015). <http://dx.doi.org/10.1038/ncomms7012>.
- [11] T. Araki, H. Tanaka, Colloidal aggregation in a nematic liquid crystal: Topological arrest of particles by a single-stroke disclination line, *Phys. Rev. Lett.* 97 (2006) 127801. <http://dx.doi.org/10.1103/PhysRevLett.97.127801>.
- [12] H.K. Bisoyi, S. Kumar, Liquid-crystal nanoscience: an emerging avenue of soft self-assembly, *Chem. Soc. Rev.* 40 (2011) 306–319. <http://dx.doi.org/10.1039/B901793N>.
- [13] C. Blanc, Colloidal crystal ordering in a liquid crystal, *Science* 352 (6281) (2016) 40–41. <http://dx.doi.org/10.1126/science.aaf4260>. URL <http://science.sciencemag.org/content/352/6281/40>. arXiv:[http://science.sciencemag.org/content/352/6281/40.full.pdf](http://arxiv.org/abs/http://science.sciencemag.org/content/352/6281/40.full.pdf).
- [14] L. Blinov, *Electro-optical and magneto-optical properties of liquid crystals*, Wiley, 1983.
- [15] H. Coles, S. Morris, Liquid-crystal lasers, *Nat. Photonics* 4 (10) (2010) 676–685.
- [16] M. Conradi, M. Ravnik, M. Bele, M. Zorko, S. Žumer, I. Mušević, Janus nematic colloids, *Soft Matter* 5 (2009) 3905–3912. <http://dx.doi.org/10.1039/B905631A>.
- [17] M. Hain, R. Glckner, S. Bhattacharya, D. Dias, S. Stankovic, T. Tschudi, Fast switching liquid crystal lenses for a dual focus digital versatile disc pickup, *Opt. Commun.* 188 (56) (2001) 291–299. [http://dx.doi.org/10.1016/S0030-4018\(01\)00989-0](http://dx.doi.org/10.1016/S0030-4018(01)00989-0). URL <http://www.sciencedirect.com/science/article/pii/S0030401801009890>.
- [18] M. Humar, I. Mušević, 3D microlasers from self-assembled cholesteric liquid-crystal microdroplets, *Opt. Express* 18 (26) (2010) 26995–27003. <http://dx.doi.org/10.1364/OE.18.026995>. URL <http://www.opticsexpress.org/abstract.cfm?URL=oe-18-26-26995>.
- [19] J.A. Moreno-Razo, E.J. Sambriski, N.L. Abbott, J.P. Hernández-Ortiz, J.J. de Pablo, Liquid-crystal-mediated self-assembly at nanodroplet interfaces, *Nature* 485 (7396) (2012) 86–89. <http://dx.doi.org/10.1038/nature11084>.
- [20] I. Mušević, M. Škarabot, U. Tkalec, M. Ravnik, S. Žumer, Two-dimensional nematic colloidal crystals self-assembled by topological defects, *Science* 313 (5789) (2006) 954–958. <http://dx.doi.org/10.1126/science.1129660>. URL <http://www.sciencemag.org/content/313/5789/954.abstract>. arXiv:[http://www.sciencemag.org/content/313/5789/954.full.pdf](http://arxiv.org/abs/http://www.sciencemag.org/content/313/5789/954.full.pdf).
- [21] I. Mušević, S. Žumer, Liquid crystals: Maximizing memory, *Nature Mater.* 10 (4) (2011) 266–268.
- [22] M. Rahimi, T.F. Roberts, J.C. Armas-Prez, X. Wang, E. Bukusoglu, N.L. Abbott, J.J. de Pablo, Nanoparticle self-assembly at the interface of liquid crystal droplets, *Proc. Natl. Acad. Sci.* 112 (17) (2015) 5297–5302. <http://dx.doi.org/10.1073/pnas.1422785112>. URL <http://www.pnas.org/content/112/17/5297.abstract>. arXiv:[http://www.pnas.org/content/112/17/5297.full.pdf](http://arxiv.org/abs/http://www.pnas.org/content/112/17/5297.full.pdf).
- [23] A.A. Shah, H. Kang, K.L. Kohlstedt, K.H. Ahn, S.C. Glotzer, C.W. Monroe, M.J. Solomon, Self-assembly: Liquid crystal order in colloidal suspensions of spheroidal particles by direct current electric field assembly (*Small* 10(2012), *Small* 8 (10) (2012) 1551–1562). <http://dx.doi.org/10.1002/sml.201290056>.
- [24] J. Sun, H. Wang, L. Wang, H. Cao, H. Xie, X. Luo, J. Xiao, H. Ding, Z. Yang, H. Yang, Preparation and thermo-optical characteristics of a smart polymer-stabilized liquid crystal thin film based on smectic Achiral nematic phase transition, *Smart Mater. Struct.* 23 (12) (2014) 125038. URL <http://stacks.iop.org/0964-1726/23/i=12/a=125038>.
- [25] M. Wang, L. He, S. Zorba, Y. Yin, Magnetically actuated liquid crystals, *Nano Lett.* 14 (7) (2014) 3966–3971. <http://dx.doi.org/10.1021/nl501302s>. pMID: 24914876. arXiv:<http://arxiv.org/abs/http://dx.doi.org/10.1021/nl501302s>.

- [26] J. Jeong, Z.S. Davidson, P.J. Collings, T.C. Lubensky, A.G. Yodh, Chiral symmetry breaking and surface faceting in chromonic liquid crystal droplets with giant elastic anisotropy, *Proc. Natl. Acad. Sci.* 111 (5) (2014) 1742–1747. <http://dx.doi.org/10.1073/pnas.1315121111>. URL <http://www.pnas.org/content/111/5/1742.abstract>. arXiv:<http://www.pnas.org/content/111/5/1742.full.pdf>.
- [27] J. Jeong, A. Gross, W.-S. Wei, F. Tu, D. Lee, P. Collings, A. Yodh, Liquid crystal janus emulsion droplets: preparation, tumbling, and swimming, *Soft Matter* (2015). <http://dx.doi.org/10.1039/C5SM01053E>.
- [28] S.V. Lishchuk, C.M. Care, Shape of an isotropic droplet in a nematic liquid crystal: The role of surfactant, *Phys. Rev. E* 70 (2004) 011702. <http://dx.doi.org/10.1103/PhysRevE.70.011702>. URL <https://link.aps.org/doi/10.1103/PhysRevE.70.011702>.
- [29] E.J. Willman, *Three Dimensional Finite Element Modelling of Liquid Crystal Electro-Hydrodynamics*, University College London, 2009.
- [30] T. Lopez-Leon, A. Fernandez-Nieves, Drops and shells of liquid crystal, *Colloid. Polym. Sci.* 289 (4) (2011) 345–359. <http://dx.doi.org/10.1007/s00396-010-2367-7>.
- [31] R.M.W. van Bijnen, R.H.J. Otten, P. van der Schoot, Texture and shape of two-dimensional domains of nematic liquid crystals, *Phys. Rev. E* 86 (2012) 051703. <http://dx.doi.org/10.1103/PhysRevE.86.051703>.
- [32] V.M.O. Batista, N.M. Silvestre, M.M. Telo da Gama, Nematic droplets on fibers, *Phys. Rev. E* 92 (2015) 062507. <http://dx.doi.org/10.1103/PhysRevE.92.062507>. URL <https://link.aps.org/doi/10.1103/PhysRevE.92.062507>.
- [33] A. DeBenedictis, T.J. Atherton, Shape minimisation problems in liquid crystals, *Liq. Cryst.* 43 (13–15) (2016) 2352–2362. <http://dx.doi.org/10.1080/02678292.2016.1209699>. arXiv:<http://dx.doi.org/10.1080/02678292.2016.1209699>.
- [34] J.K. Whitmer, X. Wang, F. Mondiot, D.S. Miller, N.L. Abbott, J.J. de Pablo, Nematic-field-driven positioning of particles in liquid crystal droplets, *Phys. Rev. Lett.* 111 (2013) 227801. <http://dx.doi.org/10.1103/PhysRevLett.111.227801>.
- [35] X. Yang, M.G. Forest, C. Liu, J. Shen, Shear cell rupture of nematic liquid crystal droplets in viscous fluids, *J. Non-Newton. Fluid Mech.* 166 (910) (2011) 487–499. <http://dx.doi.org/10.1016/j.jnnfm.2011.02.004>. URL <http://www.sciencedirect.com/science/article/pii/S0377025711000450>.
- [36] X. Yang, M.G. Forest, H. Li, C. Liu, J. Shen, Q. Wang, F. Chen, Modeling and simulations of drop pinch-off from liquid crystal filaments and the leaky liquid crystal faucet immersed in viscous fluids, *J. Comput. Phys.* 236 (2013) 1–14. <http://dx.doi.org/10.1016/j.jcp.2012.10.042>. URL <http://www.sciencedirect.com/science/article/pii/S0021999112006456>.
- [37] J. Zhao, X. Yang, J. Shen, Q. Wang, A decoupled energy stable scheme for a hydrodynamic phase-field model of mixtures of nematic liquid crystals and viscous fluids, *J. Comput. Phys.* 305 (2016) 539–556. <http://dx.doi.org/10.1016/j.jcp.2015.09.044>. URL <http://www.sciencedirect.com/science/article/pii/S0021999115006439>.
- [38] M. Mata, C.J. García-Cervera, H.D. Ceniceros, Ordering kinetics of a conserved binary mixture with a nematic liquid crystal component, *J. Non-Newton. Fluid Mech.* 212 (Supplement C) (2014) 18–27. <http://dx.doi.org/10.1016/j.jnnfm.2014.08.003>. URL <http://www.sciencedirect.com/science/article/pii/S0377025714001165>.
- [39] R.L. N6s, A.M. Roma, C.J. García-Cervera, H.D. Ceniceros, Three-dimensional coarsening dynamics of a conserved, nematic liquid crystal-isotropic fluid mixture, *J. Non-Newton. Fluid Mech.* 248 (Supplement C) (2017) 62–73. <http://dx.doi.org/10.1016/j.jnnfm.2017.08.009>. URL <http://www.sciencedirect.com/science/article/pii/S0377025716302361>.
- [40] E.G. Virga, *Variational Theories for Liquid Crystals*, Vol. 8, first ed., Chapman and Hall, London, 1994, p. 376.
- [41] A.E. Diegel, S.W. Walker, A finite element method for a phase field model of nematic liquid crystal droplets, *Commun. Comput. Phys.* (2017) (accepted).
- [42] M. Calderer, D. Golovaty, F. Lin, C. Liu, Time evolution of nematic liquid crystals with variable degree of orientation, *SIAM J. Math. Anal.* 33 (5) (2002) 1033–1047. <http://dx.doi.org/10.1137/S0036141099362086>. arXiv:<http://eprints.siam.org/doi/pdf/10.1137/S0036141099362086>.
- [43] J.W. Barrett, X. Feng, A. Prohl, Convergence of a fully discrete finite element method for a degenerate parabolic system modelling nematic liquid crystals with variable degree of orientation, *ESAIM Math. Model. Numer. Anal.* 40 (2006) 175–199. <http://dx.doi.org/10.1051/m2an:2006005>. URL [http://www.esaim-m2an.org/article\\_S0764583X06000057](http://www.esaim-m2an.org/article_S0764583X06000057).
- [44] R.H. Nochetto, S.W. Walker, W. Zhang, A finite element method for nematic liquid crystals with variable degree of orientation, *SIAM J. Numer. Anal.* 55 (3) (2017) 1357–1386. <http://dx.doi.org/10.1137/15M103844X>. arXiv:<https://doi.org/10.1137/15M103844X>.
- [45] R.H. Nochetto, S.W. Walker, W. Zhang, Numerics for liquid crystals with variable degree of orientation, in: *Symposium NN - Mathematical and Computational Aspects of Materials Science*, in: *MRS Proceedings*, vol. 1753, 2015. <http://dx.doi.org/10.1557/opl.2015.159>. URL [http://journals.cambridge.org/article\\_S1946427415001591](http://journals.cambridge.org/article_S1946427415001591).
- [46] R.H. Nochetto, S.W. Walker, W. Zhang, The ericksen model of liquid crystals with colloidal and electric effects, *J. Comput. Phys.* 352 (2018) 568–601. <http://dx.doi.org/10.1016/j.jcp.2017.09.035>. URL <http://www.sciencedirect.com/science/article/pii/S0021999117306952>.
- [47] D. Anderson, G. McFadden, A. Wheeler, A phase-field model of solidification with convection, *Physica D* 135 (12) (2000) 175–194. [http://dx.doi.org/10.1016/S0167-2789\(99\)00109-8](http://dx.doi.org/10.1016/S0167-2789(99)00109-8). URL <http://www.sciencedirect.com/science/article/pii/S0167278999001098>.
- [48] X. Tong, C. Beckermann, A. Karma, Q. Li, Phase-field simulations of dendritic crystal growth in a forced flow, *Phys. Rev. E* 63 (2001) 061601. <http://dx.doi.org/10.1103/PhysRevE.63.061601>. URL <https://link.aps.org/doi/10.1103/PhysRevE.63.061601>.
- [49] S. Torabi, J. Lowengrub, A. Voigt, S. Wise, A new phase-field model for strongly anisotropic systems, 2009 arXiv:<http://rspa.royalsocietypublishing.org/content/early/2009/02/08/rspa.2008.0385.full.pdf>, <http://dx.doi.org/10.1098/rspa.2008.0385>, URL <http://rspa.royalsocietypublishing.org/content/early/2009/02/08/rspa.2008.0385>.
- [50] N. Provatas, K. Elder, *Phase-Field Methods in Materials Science and Engineering*, Wiley-VCH, 2010.
- [51] L. Ambrosio, Existence of minimal energy configurations of nematic liquid crystals with variable degree of orientation, *Manuscripta Math.* 68 (1) (1990) 215–228. <http://dx.doi.org/10.1007/BF02568761>.
- [52] F.H. Lin, On nematic liquid crystals with variable degree of orientation, *Comm. Pure Appl. Math.* 44 (4) (1991) 453–468. <http://dx.doi.org/10.1002/cpa.3160440404>.
- [53] D.M. Anderson, G.B. McFadden, A.A. Wheeler, Diffuse-interface methods in fluid mechanics, *Annu. Rev. Fluid Mech.* 30 (1998) 139.
- [54] J. Shen, X. Yang, Numerical approximations of Allen-Cahn and Cahn-Hilliard equations, *Discrete Contin. Dyn. Syst.* 28 (4) (2010) 1669–1691.
- [55] P. Ciarlet, P.-A. Raviart, Maximum principle and uniform convergence for the finite element method, *Comput. Methods Appl. Mech. Engrg.* 2 (1) (1973) 17–31. [http://dx.doi.org/10.1016/0045-7825\(73\)90019-4](http://dx.doi.org/10.1016/0045-7825(73)90019-4). URL <http://www.sciencedirect.com/science/article/pii/0045782573900194>.
- [56] G. Strang, G. Fix, *An Analysis of the Finite Element Method*, second ed., Wellesley-Cambridge, 2008.
- [57] S. Korotov, M. Křížek, P. Neittaanmäki, Weakened acute type condition for tetrahedral triangulations and the discrete maximum principle, *Math. Comp.* 70 (233) (2001) 107–119. <http://dx.doi.org/10.1090/S0025-5718-00-01270-9>.
- [58] J.H. Brandts, S. Korotov, M. Křížek, The discrete maximum principle for linear simplicial finite element approximations of a reaction-diffusion problem, *Linear Algebra Appl.* 429 (10) (2008) 2344–2357. <http://dx.doi.org/10.1016/j.laa.2008.06.011>. URL <http://www.sciencedirect.com/science/article/pii/S0024379508003054>, Special Issue in honor of Richard S. Varga.
- [59] S.M. Wise, C. Wang, J.S. Lowengrub, An energy-stable and convergent finite-difference scheme for the phase field crystal equation, *SIAM J. Numer. Anal.* 47 (3) (2009) 2269–2288. <http://dx.doi.org/10.1137/080738143>.
- [60] J. Shen, X. Yang, A phase-field model and its numerical approximation for two-phase incompressible flows with different densities and viscosities, *SIAM J. Sci. Comput.* 32 (3) (2010) 1159–1179.
- [61] F. Alouges, A new algorithm for computing liquid crystal stable configurations: the harmonic mapping case, *SIAM J. Numer. Anal.* 34 (5) (1997) 1708–1726. URL <http://www.jstor.org/stable/2952012>.

- [62] S. Bartels, Stability and convergence of finite-element approximation schemes for harmonic maps, *SIAM J. Numer. Anal.* 43 (1) (2006) 220–238. URL <http://www.jstor.org/stable/4101259>.
- [63] J. Nocedal, S.J. Wright, *Numerical Optimization*, second ed., in: *Springer Series in Operations Research*, Springer, 2006.
- [64] S.W. Walker, FELICITY: Finite Element Implementation and Computational Interface Tool for You. URL <http://www.mathworks.com/matlabcentral/fileexchange/31141-felicity>.
- [65] S.W. Walker, FELICITY: A Matlab/C++ toolbox for developing finite element methods and simulation modeling, *SIAM J. Sci. Comput.* 40 (2) (2018) C234–C257. <http://dx.doi.org/10.1137/17M1128745>.
- [66] Y. Notay, An aggregation-based algebraic multigrid method, *Electron. Trans. Numer. Anal.* 37 (2010) 123–146.
- [67] A. Napov, Y. Notay, Algebraic analysis of aggregation-based multigrid, *Numer. Linear Algebra Appl.* 18 (3) (2011) 539–564. <http://dx.doi.org/10.1002/nla.741>.
- [68] A. Napov, Y. Notay, An algebraic multigrid method with guaranteed convergence rate, *SIAM J. Sci. Comput.* 34 (2) (2012) A1079–A1109. <http://dx.doi.org/10.1137/100818509>. arXiv:<http://dx.doi.org/10.1137/100818509>.
- [69] Y. Notay, Aggregation-based algebraic multigrid for convection-diffusion equations, *SIAM J. Sci. Comput.* 34 (4) (2012) A2288–A2316. <http://dx.doi.org/10.1137/110835347>. arXiv:<http://dx.doi.org/10.1137/110835347>.
- [70] Y. Gu, N.L. Abbott, Observation of saturn-ring defects around solid microspheres in nematic liquid crystals, *Phys. Rev. Lett.* 85 (2000) 4719–4722. <http://dx.doi.org/10.1103/PhysRevLett.85.4719>.
- [71] S. Alama, L. Bronsard, X. Lamy, Analytical description of the saturn-ring defect in nematic colloids, *Phys. Rev. E* 93 (2016) 012705. <http://dx.doi.org/10.1103/PhysRevE.93.012705>.
- [72] F. Serra, Curvature and defects in nematic liquid crystals, *Liq. Cryst.* 43 (13–15) (2016) 1920–1936. <http://dx.doi.org/10.1080/02678292.2016.1209698>. arXiv:<http://dx.doi.org/10.1080/02678292.2016.1209698>.